Ultrafast magnetization dynamics in ferromagnetic materials

Kicken, H.H.J.E.

Award date:
2005

Ultrafast magnetization dynamics in ferromagnetic materials

H.H.J.E. Kicken

February 21, 2005

Abstract

In recent magneto optical experiments (TR-MOKE) the timescale of laser induced demagnetization was found to be shorter than 0.5 ps. However, doubts have been raised if the measured signal reflects genuine loss of magnetic moment at all.

Also, for these experiments no broadly accepted theory exists. Although a few models are able to fit the data, they generally have in common that they violate or disregard conservation of angular momentum.

In this thesis both issues are addressed. First, a macroscopic model is presented to calculate the genuine magnetization dynamics from measurements of the magneto-optical Kerr effect at two different ambient temperatures. Secondly, a phonon based microscopic model is introduced to describe the laser induced demagnetization in terms of its microscopic origin, taking into account conservation of angular momentum.

This model consists of a Fermi sea of spinless electrons, and an ensemble of two level oscillators describing the phonon system. The magnetic degree of freedom of the system is described by an ensemble of two level oscillators (magnons), and treated in a mean field approximation (Weiss model).

The interactions included in the model are electron-electron scattering, electron-phonon scattering, and electron-phonon scattering with spin-flip, and these are described by Boltzmann equations. The ratio of the spin-flip and non spin-flip events is determined by the spin-flip parameter α_{sf}.

Although in literature phonon based mechanisms are generally considered to be too slow to account for the rapid demagnetization, and would take necessarily longer than electron-phonon equilibration, it was shown that the demagnetization achieved with this mechanism can be faster than e-p equilibration. Furthermore, it was shown that the demagnetization can even be faster than the thermalization time of the electron system.

Contents

List of Figures

Chapter 1

Introduction

1.1 General motivation

In modern, every day life, magnetism plays a prominent (although sometimes hidden) role. From the simple magnets, used to hold down grocery lists on the door of the refrigerator, to complicated systems like computer harddisks, magnetic materials are used for a variety of applications.

Outside of the scientific world, magnets are well understood, namely: "they stick to iron objects". However, this type of magnetism, actually called ferromagnetism (because of this behavior) displays more exotic behavior apart from "sticking to iron objects". The microscopic origin of ferromagnetism is due to an imbalance of the tiny magnetic moments of the electrons in a material, called "spins". If more spins in a material are lined up in one direction than in another, the material displays ferromagnetism (examples are iron, nickel, cobalt). This static behavior of ferromagnetism is well understood. However, the dynamic behavior of the spins is a less well understood phenomenon.

Contemporary scientific research into ferromagnetism is primarily driven by the computer harddisk industry. Schematically, a computer hard drive consists of a disk, divided into numerous very small magnetic elements, and above that a sensor, the read head, which can pick up the direction of the magnetism in each element individually. In order to make sure the information stored on the disk is rapidly accessible, the disk spins at high velocity. To give an idea of the precision involved in such a device, consider the following analogy; if you would compare a harddisk read head to a Boeing 747 airplane, and the disk to the ground, the airplane would have to fly stably only millimeters of the ground for years on end without crashing!

Because of continual demand for higher capacity, and faster access speed, these magnetic elements on the disk are made increasingly smaller, and in order to keep access times reasonable the disk revolution rates also have to be increased. This increasing miniaturization, however, leads to problems as increasingly smaller elements have to be switched increasingly faster.

In order to effectively detect the magnetization direction of a magnetic element against the background of all other elements in its vicinity, the strength of the magnetic field in the elements can be increased as their size is decreased. However, this also requires that the field used to switch the magnetization direction of the elements is also increased, increasing the chance of accidentally switching neighboring elements.

This problem can be overcome by a phenomenon discovered by Pierre Curie in the late nineteenth century; he discovered the effect that the magnetic field exhibited by the ferromagnet decreases with increasing temperature, and recovers its magnetic field when cooled again. Thus, by heating the magnetic element, the required switching field may be much lower, decreasing the chance of accidental switching. This process, called heat assisted switching, is currently investigated in the hard drive industry.

Because of the small size of the magnetic elements on a harddisk, the heating of these elements must be local and very precise. In order to accomplish this feat, a laser can be used.

However, the usage of lasers raises also new questions.

In this thesis, some of the questions concerning the laser induced demagnetization process will be investigated.

1.2 Fast magnetization dynamics

Since the experiments of Pierre Curie, in the late nineteenth century, it is known that the magnetization of a ferromagnetic material diminishes when it is heated, and even completely disappears at a critical temperature, known as the Curie temperature. When this heating occurs by a high power laser pulse, one expects this same behavior, taking place at the site of the laser spot. In pioneering experiments by Beaurepaire *et al.*[1] in 1996, it was shown that this process is extremely rapid, and takes place on a timescale shorter than 1 ps. Recently, more precise measurements have been made by van Kampen *et al.*[2], revealing the timescale of the demagnetization process to be faster than 0.5 ps. So far no accepted theory has been found yet that accounts for this extremely short timescale, and doubts have even been raised if the measured signal reflects genuine loss of magnetic moment at all.

More recently more measurements of this type have been made by various groups, using different materials and in different regimes. In this thesis we will focus on one of these experiments, namely the measurements of van Kampen *et al.*[2].

Van Kampen *et al.* have performed temperature dependent measurements on nickel thin films at ambient temperatures. They measured the Magneto-Optical (MO) contrast after pulsed laser heating (see section 2.1) as a function of time at three different ambient temperatures, giving data for an optical artefact elimination scheme which will be described and extended in chapter 3. They used pump powers, heating the sample locally to about 100 K above the ambient temperature (well below the Curie point), giving rise to a decrease in magnetization of about 5%.

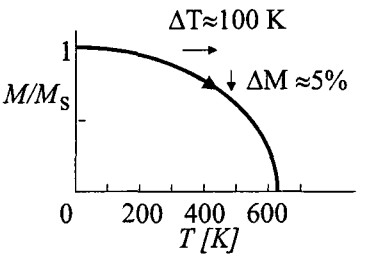

Figure 1.1: Temperature range of the measurements of van Kampen *et al.* (schematic). Using 100 fs. laser pulses around room-temperature, van Kampen *et al.* heat a thin nickel film approximately 100 K, reducing the sample's magnetization by approximately 5%.

At this time there are two main problems in this field

1. The Magneto-Optical Kerr Effect (MOKE) with which these extraordinary data were measured is not easily interpreted, and strong suspicions exist that at least in the first couple of hundred femtoseconds the signal is not purely magnetic. This is expected due to the non-equilibrium state of the electronic system, caused by the absorbtion of a high power laser pulse.

2. The microscopic origin of the ultra-fast demagnetization process is not yet understood. Although there are some models available, these models have in common that they violate or disregard conservation of angular momentum.

The outline of this report is as follows; in chapter 2 some background information on magneto-optics and fast magnetization dynamics will be presented. Chapter 3 focusses on a macroscopic

model (dealing with problem 1), which gives a route to the extraction of the genuine magnetization data from MOKE-dynamics. Finally, in chapter 4 a model (dealing with problem 2) is presented to explain laser induced ultra-fast demagnetization in terms of its microscopic origin.

Chapter 2

Background on magneto-optics

2.1 Magneto-optical Kerr effect

In isotropic or highly symmetric materials the dielectric displacement, $\vec{D}$, is related to the electric field, $\vec{E}$, by the well known formula

$$\vec{D} = \epsilon \vec{E}, \tag{2.1}$$

with ϵ the dielectric constant. However, in ferromagnetic materials, symmetry is broken because of the finite magnetization of the sample. In this more complicated situation the dielectric constant is no longer a good description and is replaced by the dielectric tensor $\bar{\bar{\epsilon}}$

$$\vec{D} = \bar{\bar{\epsilon}} \vec{E}. \tag{2.2}$$

Because of the off-diagonal elements in the dielectric tensor, a linearly polarized laser beam, which is reflected of a magnetic sample, is changed with respect to its rotation and ellipticity. The induced changes are dependent on the magnetization of the sample due to the magnetization dependencies of the off-diagonal elements. This makes this effects an excellent method to measure magnetization on very short timescales.

If the magnetization of the sample is parallel to the z-axis, the dielectric tensor can be written as [2]

$$\bar{\bar{\epsilon}} = \begin{bmatrix} \epsilon_{xx} & \epsilon_{xy} & 0 \\ -\epsilon_{xy} & \epsilon_{xx} & 0 \\ 0 & 0 & \epsilon_{xx} \end{bmatrix}, \tag{2.3}$$

with ϵ_{xx} and ϵ_{xy} being in general complex. Because of the off-diagonal elements ϵ_{xy} an electric field in the x-direction induces a polarization in the y-direction. Therefore, after reflection from the sample, the originally linearly polarized light will display a certain ellipticity and the polarization axis will be rotated. The polarization state $\tilde{\Theta}$ can be written as $\tilde{\Theta} = \Theta' + \mathrm{i}\Theta''$, with Θ' the polarization rotation, and Θ'' the polarization ellipticity. At perpendicular incidence Θ can also be written as

$$\tilde{\Theta} = \tilde{F} M_z, \tag{2.4}$$

with $\tilde{F}$ a complex constant, the generalized Fresnel factor, and M_z the magnetization in the z-direction. By measuring $\tilde{\Theta}$ we can gain information about the magnetization of the sample.

The microscopic origin of the Kerr effect lies in the collaboration of optical selection rules and spin-orbit coupling. For circularly polarized light only transitions with $\Delta l = \pm 1$ and $\Delta m_l = \pm 1$ are allowed, which makes the effect particularly sensitive to the changes in the electrons' orbital momentum. Since spin-orbit coupling induces interaction between $\vec{L}$ and $\vec{S}$, the spin system can be probed through the selection rules for orbital angular momentum. The transitions available for probing by optical techniques depend on the photon energy and the band-structure of the material. This makes that interpreting the probe signal in a non-equilibrium situation, i.e. right after excitation by an intense laser pulse, is not straightforward; in particular one could expect a non-magnetic contribution due to changes in the occupation of states.

2.2 Laser-induced magnetization dynamics

In order to measure ultra-fast demagnetization first the demagnetization process has to be initiated, and then the spin system has to be probed in a time-resolved way. The demagnetization process is induced by firing a high power laser beam (pump pulse) at the sample, and thus locally heating it, subsequently losing part of its magnetization. After a short time-interval, a second, low power (ratio with respect to the pump beam is approximately 1:20) laser beam, the probe pulse, is fired at the target. By varying the time-interval at which the probe beam hits the sample, a time-resolved method (TR-MOKE) of measuring magnetization at the resolution of the risetime of the laserpulses is obtained (see figure 2.1).

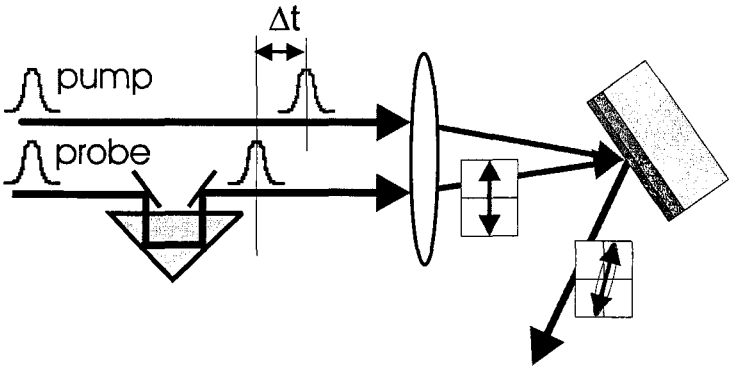

Figure 2.1: Schematic depiction of a TR-MOKE setup. The high power pump laser pulse (red) strikes the sample, and heats a piece of ferromagnetic material, inducing an ultra-fast decrease of the magnetization. After a short delay, of the order of the risetime of the laser pulses, a second low power linearly polarized (probe) laser pulse (blue) hits the sample. The polarization state of this probe pulse is changed in a magnetization dependent fashion, giving an indication of the current average magnetization at the laser spot.

2.3 Three temperature model

The three temperature model (3TM), introduced by Beaurepaire *et al.*[1], describes the properties and interactions of a ferromagnetic system in a phenomenological way; The system is divided into three subsystems: electrons, lattice and spins, and each of the subsystems is assigned a temperature. For the electronic system, and lattice system this is relatively straightforward, because of well known heat capacities. For a free electron gas the electronic heat capacity, c_e, is given by [3]

$$c_e = \gamma T_e = \frac{1}{2}\pi N k_B T_e / T_F, \tag{2.5}$$

with T_e the electron temperature, k_B Boltzmann's constant, and T_F the Fermi-temperature, which is a material parameter. However, when the electronic system is not in equilibrium this not a valid quantity, therefore thermalization is neglected.

For the lattice system the Debye approximation for phonons (lattice vibrations) can be used to find the lattice heat capacity c_l [3]

$$c_l = 9Nk_B \left(\frac{T_l}{\Theta}\right)^3 \int_0^{x_D} \mathrm{d}x \frac{x^4 e^x}{(e^x - 1)^2}, \tag{2.6}$$

with T_l the lattice temperature, Θ the Debye-temperature for which the same argument as the Fermi-temperature applies, and $x_D = \Theta/T_l$. At low temperatures this equation simplifies to the famous Debye T^3 law, at temperatures above the Debye temperature (ambient temperature regime) the heat capacity is approximately constant.

For the spin system the temperature is defined by the well known magnetization versus temperature curve, displayed in figure 2.2. In this way (naively interpreting the MOKE-angle as a purely magnetic signal) the model can be used to fit the measurements.

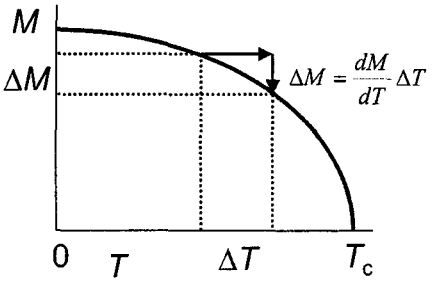

Figure 2.2: For small variations in the magnetization, the curve is nearly linear and the (spin)temperature can be defined as $\Delta M = \frac{\mathrm{d}M}{\mathrm{d}T}\Delta T_s$

The model is shown schematically in figure 2.3. The interaction with the laser field proceeds trough the electrons, and since only very few optical transitions will induce a net spin change, only the electron system will be heated. The other two systems are coupled to the electron system and to each other through different kinds of relaxation mechanisms. These interactions can be represented by a system of coupled differential equations

$$c_e(T_e)\frac{\partial T_e}{\partial t} = -g_{el}(T_e - T_l) - g_{es}(T_e - T_s) + P(t), \tag{2.7}$$

$$c_l(T_l)\frac{\partial T_l}{\partial t} = -g_{el}(T_l - T_e) - g_{sl}(T_l - T_s), \tag{2.8}$$

$$c_s(T_s)\frac{\partial T_s}{\partial t} = -g_{es}(T_s - T_e) - g_{sl}(T_s - T_l), \tag{2.9}$$

where $c_i(T_i)$ is the heat capacity of system i, $P(t)$ is the laser source term, and g_{ij} is the coupling constant between systems i and j. T_e is the electron temperature, T_l is the lattice temperature, and T_s the spin-temperature. These equations can be somewhat simplified. First for a temperature close to or above the Debye temperature the lattice heat capacity can be considered constant; Second, from experimental work [2] it is found that the spin-temperature seems to follow the electron temperature very closely, suggesting a negligible heat capacity of the spin system. Therefore, the $g_{sl}(T_s - T_l)$ and $g_{es}(T_e - T_s)$ terms will be of little importance, and the electron temperature can be considered to be the dominant mechanism for demagnetization. This means that the electron and lattice temperatures will be almost unaffected by the spin-temperature. Therefore we can use a simplified three temperature model (S3TM) [2]

$$c_e(T_e)\frac{\partial T_e}{\partial t} = -g_{el}(T_e - T_l) + P(t), \tag{2.10}$$

$$c_l\frac{\partial T_l}{\partial t} = g_{el}(T_e - T_l), \tag{2.11}$$

$$\frac{\partial T_s}{\partial t} = \tau_M^{-1}\left[T_e(t) - T_s(t)\right]. \tag{2.12}$$

The electron and lattice temperatures are now coupled as they would be in a system without magnetization, but a spin-system is added, which follows the electron temperature with a characteristic delay τ_M. It is important to keep in mind that the electron-temperature is only a valid quantity after electron thermalization, i.e. when the electrons are in a Fermi-Dirac distribution. Before this time ($\approx$ 100 fs) the electron-temperature can be thought of as the excess energy in the system.

Because of the $c_e(T_e) = \frac{1}{2}\pi N k_B T_e/T_F = \gamma T_e$ (for a free electron gas) term in eq. 2.10, the equations are not homogeneous, and cannot be solved analytically. Therefore a numerical approach is required.

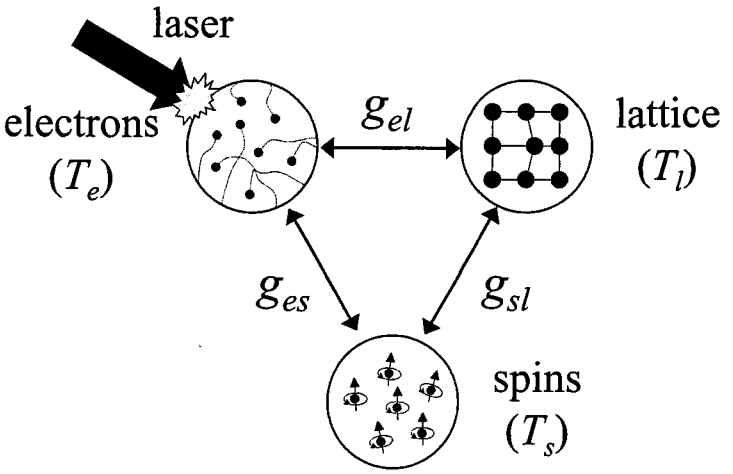

Figure 2.3: Three temperature model; a magnetic system is split into three subsystems, and each is assigned a temperature and heat capacity. The energy-exchange is governed by coupling constants g_{ij}, with i, j representing one of the subsystems. The laser field only interacts with the electron system, assuming equal amounts of left and right polarized light. interactions between subsystems then equilibrate their temperatures. The spin-temperature is defined by the equilibrium $M(T)$ relation, i.e. the higher the spin-temperature, the lower the magnetization.

A numerical simulation using the S3TM-equations (temperature vs. pump-probe delay time) is displayed in figure 2.4. The laser dissipates all energy in the electron system, so a rapid increase of the electron temperature is seen, but because the temporal width of the laserpulse, the energy is not instantly delivered to the electron system. It is clearly visible that the electron temperature is the "driving force" in the model, with the spin temperature closely following on a characteristic time (τ_M).

After the sudden increase of the electron temperature the systems equilibrate with a characteristic time τ_E, the electron-lattice equilibration time. When the systems are equilibrated (after approximately 4 ps), information about the heat capacities can be extracted. First, from the ratio of the temperature differences ΔT_1 and ΔT_2 (defined in figure 2.4), the ratio of the electron and lattice heat capacities can be found. The bigger temperature difference ΔT_1, the smaller the heat capacity of the electron system, and the same goes for ΔT_2 and the lattice heat capacity.

The parameter τ_E can be related to the electron-lattice coupling constant and the heat capacities of the electron and lattice systems [2].

$$\tau_E = \frac{c_e c_l}{c_e + c_l} g_{ep}^{-1} \tag{2.13}$$

For completeness we introduce a third time constant, the thermalization time τ_{th}. It is defined as the time necessary for the electron system reform a Fermi-dirac distribution after the intens laser pulse has disturbed the system. In the S3TM, τ_{th} is zero by definition. However, the time constant is indicated in figure 2.4 as an example. In this case the "thermalization time" indicated is actually caused by the temporal width of the laser pulse, described by a gaussian

$$P(t) = \frac{E_p}{w_p} e^{-\left(\frac{t}{w_p}\right)^2} \tag{2.14}$$

with E_p the (pump) laser energy, and w_p the temporal width of the pulse.

The characteristic timescales $\tau_{th}, \tau_M, \tau_E$ can be extracted from the transients by fitting the

curves with exponential functions.

$$\Delta T_e(\Delta t) = \Delta T_1\left[1-e^{\left(-\frac{\Delta t}{\tau_{th}}\right)}\right]e^{\left(-\frac{\Delta t}{\tau_E}\right)} + \Delta T_2\left[1-e^{\left(-\frac{\Delta t}{\tau_E}\right)}\right] \quad (2.15)$$

$$\Delta T_l(\Delta t) = \Delta T_2\left[1-e^{\left(-\frac{\Delta t}{\tau_E}\right)}\right] \quad (2.16)$$

$$\Delta T_s(\Delta t) = \Delta T_1\left[1-e^{\left(-\frac{\Delta t}{\tau_M}\right)}\right]e^{\left(-\frac{\Delta t}{\tau_E}\right)} + \Delta T_2\left[1-e^{\left(-\frac{\Delta t}{\tau_E}\right)}\right] \quad (2.17)$$

In general the values for τ_E will differ a few percent according to which transient ($T_e(t)$, $T_l(t)$) is fitted. A good approximation to this fitting is to estimate the delay time at half the peak value.

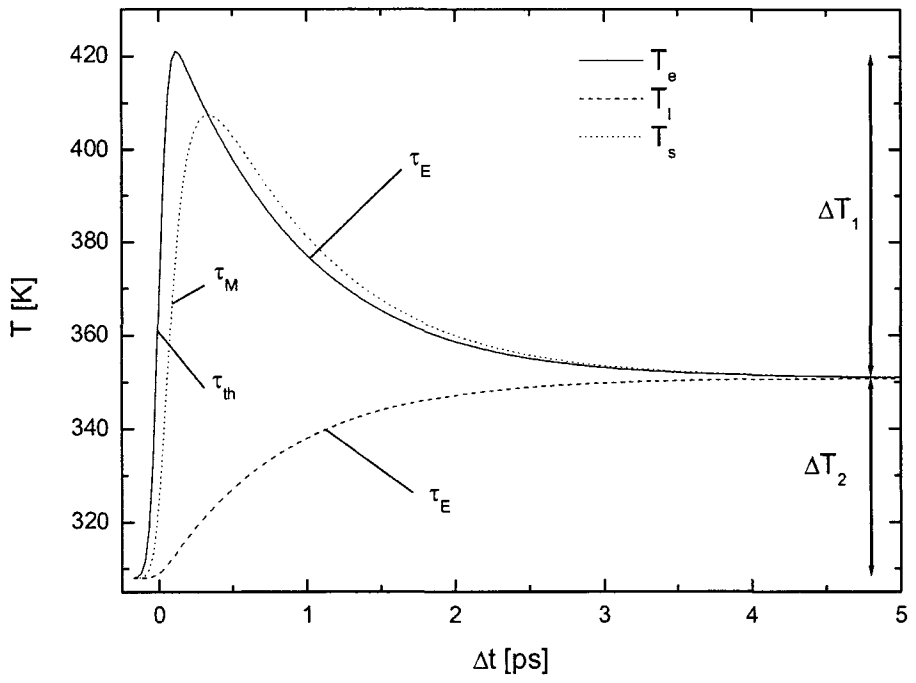

Figure 2.4: Electron (T_e), lattice (T_l) and spin-temperature (T_s) transients, calculated with the simplified three temperature model.

In figure 2.5 a measurement made by Beaurepaire *et al.*, is displayed. These measurements can easily be fitted with the three temperature model, and some information on the coupling constants and heat capacities can be found. However, from this model no information on the actual physics can be extracted. Also, conservation of angular momentum is completely disregarded, because only energy flow is considered. This is of crucial importance, as will be shown in section 4.1. If one interprets the Kerr-angle as a purely magnetic signal, figure 2.5 shows a change in magnetization of almost 50% within a picosecond. This remarkable result shows that the demagnetization process is faster than what any accepted microscopic theory predicts (see section 4.1.1). However, since time dependent optical artifacts (bleaching, state-filling), can be hidden by the complex constant $\tilde{F}$ in equation 2.4, the interpretation of the MOKE-signal is non-trivial and there have been some doubts as to the MOKE-signal showing magnetism at all!

Recently, measurements by van Kampen *et al.*[2] have shown that for nickel films the static MOKE-measurements at different ambient temperatures are consistent with more accomplished methods (SQUID) of measuring the magnetization. Also, a scheme was proposed to eliminate the optical artifacts, which we will follow and expand to an iterative scheme (see chapter 3) to

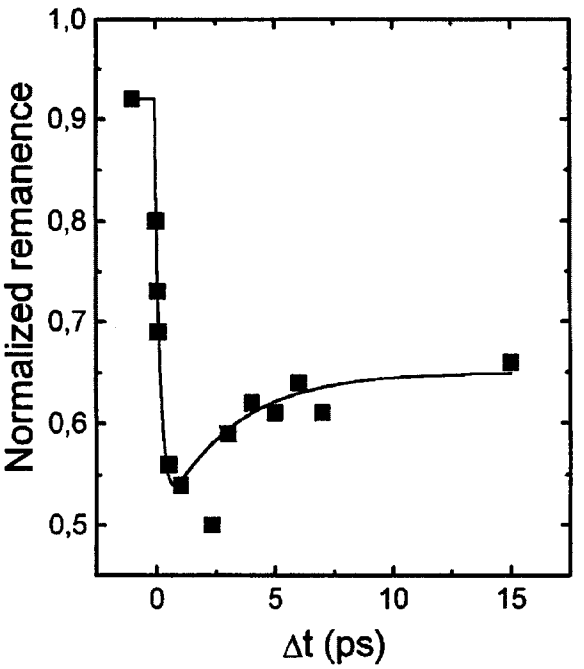

Figure 2.5: Results of pump-probe measurements by Beaurepaire *et al.* on a nickel film using 60 fs laser pulses. The remanent magnetization shown, derived from the magneto-optic Kerr effect is plotted as a function of the delay time Δt between pump and probe pulse. It shows a rapid decrease of the magnetization within approximately one picosecond. Reproduced from Ref.[1].

extract the magnetic signal from the TR-MOKE data.

2.4 Summary

A laser beam, reflected off a piece of ferromagnetic material, is changed with respect to its polarization direction and ellipticity. This change is due to the magnetization dependence of the dielectric tensor. Because the probed transitions depend strongly on the photon energy used, and the band structure of the material, interpretation of the measured signal is not trivial, in particular in non-equilibrium conditions, when the occupation of states may be very different.

Using this effect (magneto-optical Kerr effect) and very short laser pulses it is possible to measure magnetization in a time resolved method fashion.

To extract characteristic timescales such as the demagnetization time, a thermodynamic (three temperature) model was introduced by Beaurepaire *et al.* and simplified by van Kampen *et al.* This model can be used to fit the measured data, however, it does not yield any information on the actual physics, nor does it consider conservation of angular momentum, which is of crucial importance.

Chapter 3

Macroscopic Model

Without going into an ab initio calculation of the MOKE-response[4], a phenomenological approach can be taken to get magnetization data from TR-MOKE transients. In this chapter a method is introduced that follows van Kampen *et al.* and eventually ends up with a scheme that is able to calculate a magnetic signal from the MOKE-dynamics.

3.1 Optics vs. Magnetism

As already sketched in section 2.1 the MOKE-signal cannot be interpreted as being simply proportional to the magnetization; especially in the first 100 fs a significant contribution from optical effects, such as bleaching, is expected, because of the non-equilibrium state of the electrons. The absorbtion of a high power laser pulse, can result in the depopulation of the lower energy levels of an optically allowed transition, effectively making the material transparent for photons of the energy associated with this transition.

As also discussed in section 2.1, the optical effects are described by the complex constant $\tilde{F}$ in equation 2.4. However, in general these artifacts are time- and (slightly) temperature-dependent, which further complicates the interpretation of the TR-MOKE dynamics. We can write analogously to equation 2.4

$$\tilde{\Theta}(t,T) = \tilde{F}(t,T)\, M(t,T), \tag{3.1}$$

with $\tilde{\Theta}(t,T)$ the complex polarization state, $M(t,T)$ the magnetization, and $\tilde{F}(t,T)$ a complex function describing optical effects such as bleaching (generalized Fresnel factor).

In the next sections we present a route which leads from a naive interpretation of the MOKE-angle being directly proportional to the magnetization signal, to a more refined interpretation that accounts for an explicit time dependence of $\tilde{F}$. An iterative method to achieve this will be developed.

3.2 Introduction of a thermal difference scheme

It has been a long standing issue to separate the true magnetization dynamics ($M(t,T)$) from the magneto optical artifacts ($\tilde{F}(t,T)$). A thermal difference scheme has been proposed to accomplish this separation [2]. In such a scheme the weak temperature dependence of the optical artifacts is exploited to equate the thermal difference of the measured MO response to the thermal difference of the magnetization dynamics. We will start with a brief explanation of the scheme, followed by a more formal approach leading to an iterative method.

Let us first look at the general relation of equation 3.1. In a weak perturbation limit the transient MO response can be described by a lowest order expansion of the pump-induced effects

$$\Delta\tilde{\Theta}(t,T) = M_0(T)\,\Delta\tilde{F}(t,T) + \tilde{F}_0 \Delta M(t,T), \tag{3.2}$$

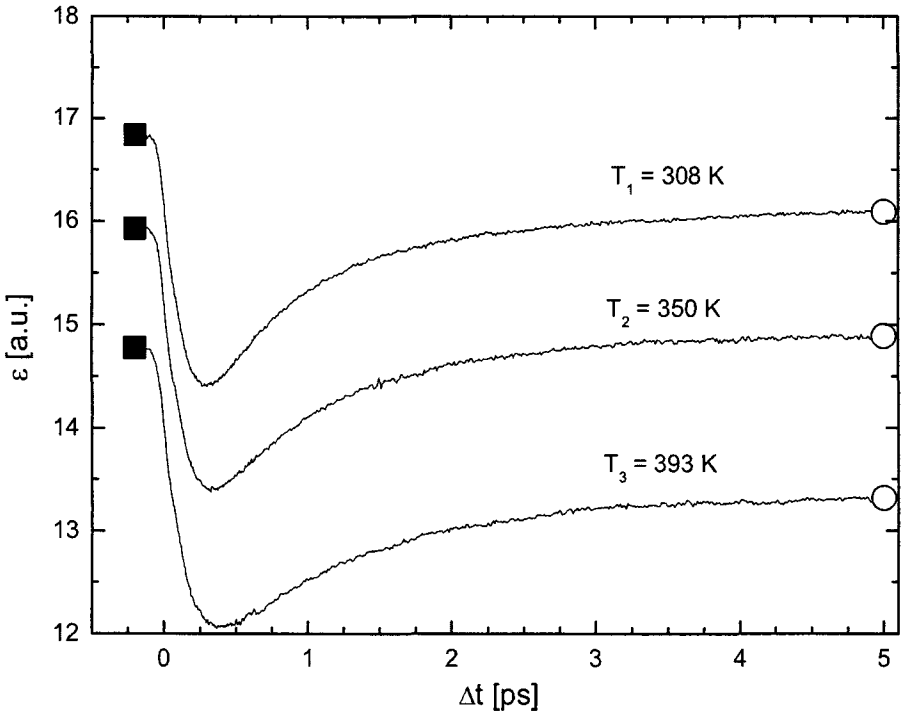

Figure 3.1: MOKE-transients of a thin nickel film; ellipticity versus delay-time at three different ambient temperatures. The measurements begin at the black squares on the left-hand side of the picture. initially, when the sample is heated by the pump-pulse, the signal drops rapidly to a minimum around 0.4 ps, and then recovers slowly while the sample is cooling down again. reproduced from ref. [2]

where Δ is used to denote the pump-induced effects, $M_0(T)$ and $\tilde{F}_0$ represent the magnetization and optical signals, respectively, at $t = 0$. The linearization of $\tilde{F}(t,T)$ is only valid for small pump-induced changes, and the cross-term $\Delta\tilde{F}(t,T)\Delta M(t,T)$ is neglected.

This equation gives us somewhat more to work with, because we already know some of its limits. $M_0(T)$ can be determined by other methods, and it has been found that the static MOKE-response is consistent with SQUID-measurements, i.e. equilibrium magnetization versus temperature behavior is the same for static MOKE and SQUID. This gives the boundary condition $\Delta\tilde{F}(t \rightarrow \infty, T) = 0$, i.e. the pump-induced effects decay within a finite timespan (typically tens of picoseconds). Also, before a laserpulse has perturbed the sample, the measured signal must give the magnetization on the same grounds, so $\Delta\tilde{F}(t \leq 0, T) = 0$.

Figure 3.1 displays a typical measurement of the MOKE-signal for three different ambient temperatures. Plotted is the ellipticity of the polarization of the reflected probe beam as a function of the delay time between pump and probe pulse. There is a clear temperature dependance visible.

First, there is an overall difference between the curves of the measurements at different ambient temperatures. The differences among these points is readily derived from the equilibrium magnetization vs. temperature curve (see figure 3.2).

The three curves present qualitatively the same behavior. The curves drop sharply at $\Delta t = 0$ to reach their minimum at about $\Delta t \approx 400$ fs, and then slowly recover to their initial value (not completely shown here). In a naive interpretation ($\epsilon \propto$ magnetization), at $\Delta t = 0$ when the sample is heated, the sample loses part of its magnetization until the dissipation of heat

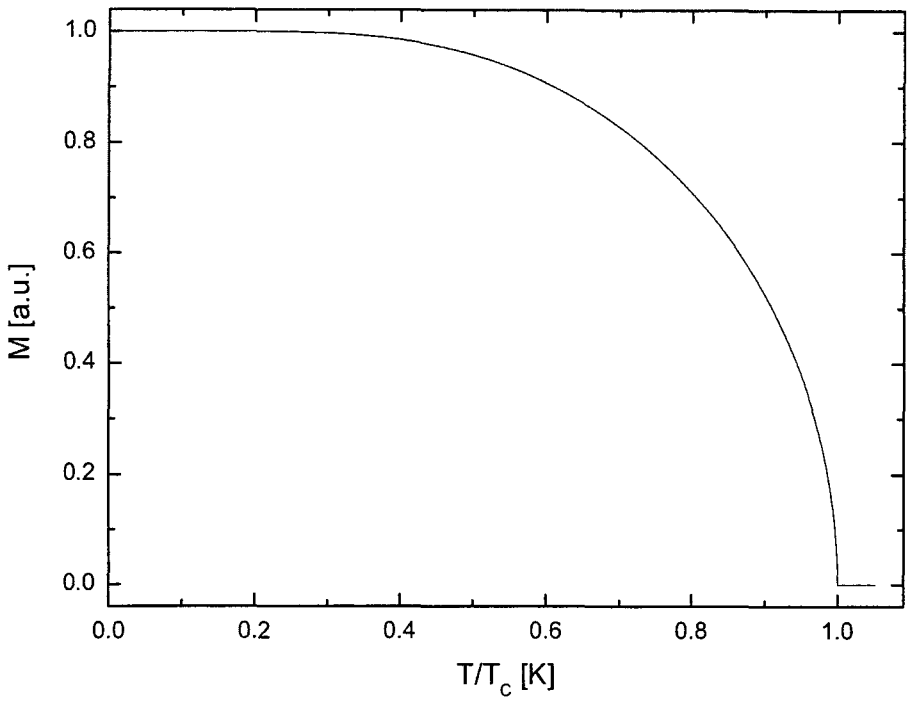

Figure 3.2: Equilibrium magnetization versus temperature in the Weiss (mean or molecular field approximation) model for magnetization. The magnetization decreases as a function of temperature, with increasingly steeper slope. At approximately 575 K, for this case, a critical point (Curie temperature) is encountered. Above this temperature no more ferromagnetic behavior is encountered.

to the substrate and environment begins to cool the sample at $\Delta t \approx 400$ fs, recovering the magnetization.

A more accurate analysis shows that there are some small differences among the curves. Mainly, the values at $t = 0$, and the depth of the minimum differ. These difference are also easily attributed to the dependence of the magnetization on the temperature. Secondly, a slight broadening of the minimum is observed. In terms of the (S)3TM this broadening of the minimum can be attributed to the increase of the electronic heat capacity; at higher temperatures c_e is higher, and it takes longer to transfer energy from the electron system to the lattice.

This qualitative analysis of figure 3.1 leads to the assumption that the optical effects will only be very weakly dependent on temperature. Also, on physical grounds, it is quite clear that the changes in the electronic system (Fermi-Dirac distribution) due to the increased ambient temperature will be minor in comparison with the effect of the pump laser pulse. An ambient temperature rise of 100 K will induce only changes in the electron system in the order of meV. In contrast, a laser pulse will deposit an energy in the order of eV in a much smaller band of energy levels.

Normalizing eq. 3.2 to the equilibrium value $\Theta_0 = \Theta(t = 0, T) = \tilde{F}_0 M_0$ leads to

$$\frac{\Delta\tilde{\Theta}(t,T)}{\Theta_0(T)} = \frac{\Delta\tilde{F}(t)}{\tilde{F}_0} + \frac{\Delta M(t,T)}{M_0(T)}. \tag{3.3}$$

If we now take the thermal difference at two different ambient temperatures (T_0 and T_1, with

$T_1 > T_0$), the optical artifacts disappear due to their weak temperature dependence

$$\left.\frac{\Delta\tilde{\Theta}(t,T)}{\Theta_0(T)}\right|_{T_1} - \left.\frac{\Delta\tilde{\Theta}(t,T)}{\Theta_0(T)}\right|_{T_0} = \left.\frac{\Delta M(t,T)}{M_0(T)}\right|_{T_1} - \left.\frac{\Delta M(t,T)}{M_0(T)}\right|_{T_0}, \tag{3.4}$$

with T_0 and T_1 denoting the ambient temperature at which an experiment takes place ($T_1 > T_0$). This gives a method to get rid of the optical artifacts, but the magnetization behavior at a single ambient temperature still remains unsolved.

There is experimental proof of equation 3.4 being accurate (see figure 3.3). Van Kampen *et al.*[2] have measured the rotation (ψ') and the ellipticity (ψ'') as a function of pump-probe delay time at two ambient temperatures. The $'$ is used to denote rotation, and the $''$ is used to denote ellipticity. Using this scheme, the thermal differences of these signals (δ', δ'') were computed, as well as the generalized Fresnel factors ($\Delta F'$, $\Delta F''$), which can be calculated by taking the right linear combination of the TR-MOKE signals at the two different ambient temperatures.

$$\frac{\Delta\tilde{F}(t)}{\tilde{F}_0} = \frac{1}{r-1}\left.\frac{\Delta\tilde{\Theta}(t,T)}{\Theta_0}\right|_{T_1} - \frac{r}{r-1}\left.\frac{\Delta\tilde{\Theta}(t,T)}{\Theta_0}\right|_{T_0}, \tag{3.5}$$

with

$$r = \frac{\left.\frac{\Delta M(t,T)}{M_0}\right|_{T_1}}{\left.\frac{\Delta M(t,T)}{M_0}\right|_{T_0}}. \tag{3.6}$$

Consequently $\frac{\Delta\tilde{F}(t)}{F_0}$ vanishes when $r = 1$, i.e. when the two pump-induced magnetization traces are equal.

The rotation and ellipticity transients have the same microscopic origin, however, they show very different dynamics. Clearly visible is the fact that the thermal difference of the ellipticity and rotation, represented by δ' and δ'' respectively, show identical dynamics. This is expected because the separation scheme was designed such that δ' and δ'' should represent the changing magnetization of the sample.

Also, the time at which the maximum of the demagnetization effect occurs is shifted to longer timescales as compared to the original data. In the original data the maximum occurs at approximately 250 fs., while it now occurs at approximately 500 fs. This shift seems to suggest that the genuine demagnetization is slower than the drop in MO contrast.

While this separation scheme already seems a good result, there are some problems with this interpretation. In the separation approach all the changes in the signal due to temperature dependence of the heat capacities of the systems were neglected. Also, in figure 3.3(d), it is visible that the calculated generalized Fresnel factors continue to contribute for at least 2 ps. In the case of the polarization rotation ($\Delta F'/F'$), the prolonged existence of the optical effects would even raise doubts if the optical contribution would even decay at all.

The non-zero values of the generalized Fresnel factors are expected to be the result of the non-equilibrium state of the electronic system. However, the electron thermalization is completed within the first 100 fs. These findings leaves two possible conclusions; first, the optical effects are exaggerated by the calculation. Secondly, they originate from long living occupations in the band structure, i.e. the band structure contains bottlenecks of some sort, which prevent the excited electrons from filling their equilibrium states on this timescale.

3.3 Generalized thermal difference scheme

To go another step further we switch variables and introduce a spin temperature $T_s(t)$, which is linked to the magnetization by the well known magnetization versus temperature curve, as in

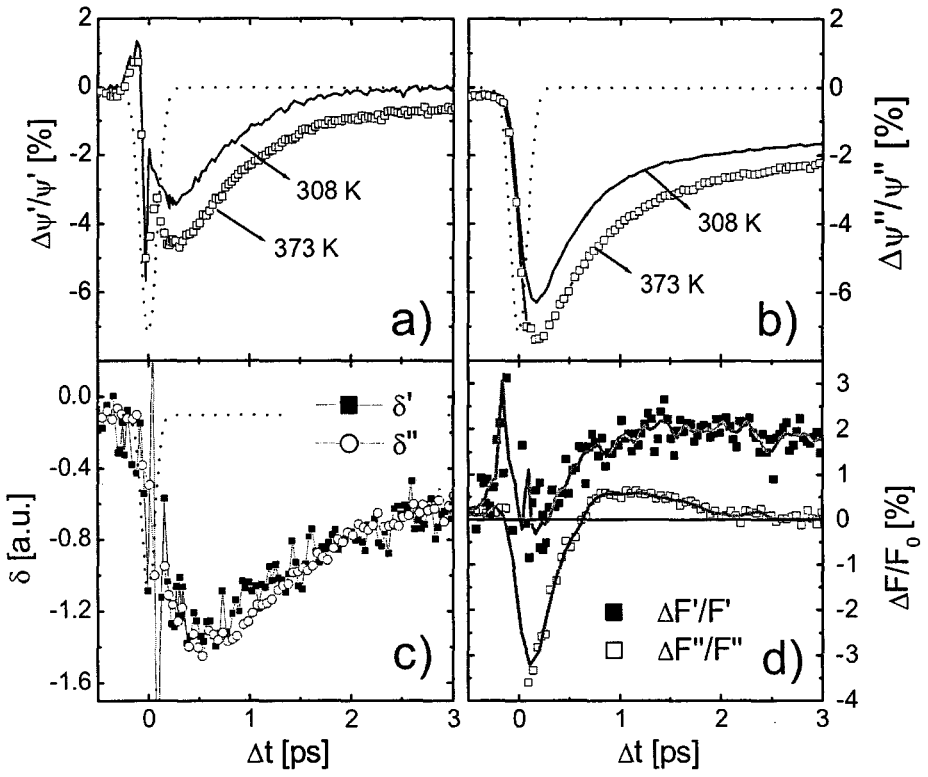

Figure 3.3: (a) rotation and (b) ellipticity measurements at ambient temperatures of 308 K and 373 K measured on a nickel thin film. (c) The thermal difference of the rotation (squares) and ellipticity (circles). (d) Calculated optical effects using equation 3.5, solid lines are curves intended as guide to the eye. Reproduced from ref. [2]

the (S)3TM (see figure 2.2). For small temperature variations we can write:

$$M(T_s(t)) = M_0 + \frac{\mathrm{d}M}{\mathrm{d}T}\Delta T_s(t) \text{ , and} \tag{3.7}$$

$$\Delta M(T_s(t)) = \frac{\mathrm{d}M}{\mathrm{d}T}\Delta T_s(t). \tag{3.8}$$

The MOKE-traces can now be converted into spin-temperature curves (see figure 3.4). By substituting equation 3.8 into equation 3.2, neglecting the pump induced generalized Fresnel factors and rewriting we obtain

$$\Delta T_s(t) = \frac{\Delta\tilde{\Theta}(t,T)}{F_0\frac{\mathrm{d}M}{\mathrm{d}T}}. \tag{3.9}$$

The data from figure 3.4(a) ($\Delta\Theta(t,T)$) and (b) ($\frac{\mathrm{d}M}{\mathrm{d}T}$) are then used to produce (c).

Notice that the order of the curves is completely reversed; as the curve at an ambient temperature of 393 K had the deepest minimum in figure 3.1, it now has the lowest maximum in figure 3.4. This is due to the increasing derivative of the magnetization curve which occurs in the above equations. The difference in the maxima of the curves at various ambient temperatures is now readily attributed to the change in the electron heat capacity ($c_e = \gamma T_e$). Since optical artifacts are weakly temperature dependent, they cannot be the cause of this difference.

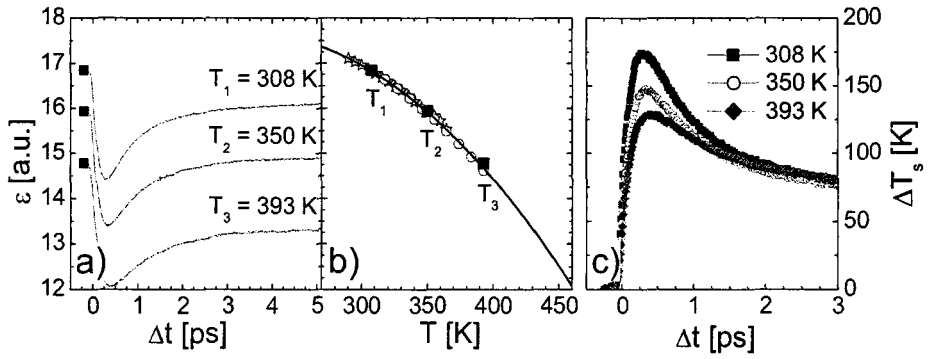

Figure 3.4: Calculated spin-temperatures, using equations (3.2) and (3.8). (a) the ellipticity transients from figure 3.1 (b) equilibrium magnetization versus temperature; the black squares represent the points indicated in (a). The black curve is a quadratic fit to data obtained by static measurements of the Kerr effect, and SQUID. (c) Pump induced spin temperature versus pump-probe time delay. The minima of (a) transform into the maxima of (c). Due to the steepness of the magnetization curve in (b) the deepest minimum in (a) (highest ambient temperature) results in the lowest maximum. The shown ambient temperature dependence is readily attributed to a near linear increase of the total heat capacity. Reproduced from ref.[2]

Using the spin temperature equations it can be shown where the thermal difference method went astray. After substituting 3.8 into equation 3.2 we obtain

$$\Delta\tilde{\Theta}(t,T) = M_0\Delta\tilde{F}(t,T) + \tilde{F}_0\frac{\mathrm{d}M}{\mathrm{d}T}\Delta T_s(t). \tag{3.10}$$

Then, expanding this equation in a thermal difference leads to

$$\delta\left[\Delta\tilde{\Theta}(t,T)\right] = \delta\left[M_0\right]\Delta\tilde{F}(t,T) + \delta\left[\frac{\mathrm{d}M}{\mathrm{d}T}\right]\tilde{F}_0\Delta T_s(t) + \frac{\mathrm{d}M}{\mathrm{d}T}\tilde{F}_0\delta\left[\Delta T_s\left(t\right)\right], \tag{3.11}$$

where we introduced the $\delta[...]$ notation to indicate a thermal difference, i.e. $\delta\left[...\right] = ...|_{T_1} - ...|_{T_0}$. We assume that the temperatures T_0 and T_1 are close enough to make the thermal differences δ a small parameter, which allows for the linear expansion in equation 3.11. We also made use again of $\delta\left[\tilde{F}\right] = 0$.

With respect to the previous thermal difference method, this scheme has two main advantages. First, it explicitly takes into account the non-constant behavior of the equilibrium magnetization. Second, this time it is possible to calculate the actual spin temperature (and thus magnetization transient) instead of the thermal difference.

These equations would now be solvable for $\Delta T\left(t\right)$, if not for the $\delta\left[\Delta T_s(t)\right]$ term, so we will assume that $\delta\left[\Delta T_s(t)\right] = 0$ (as done implicitly in the thermal difference method of section 3.2). This assumption corresponds to the curves of figure 3.4(c) being exactly the same, i.e. the heat capacity of the system is constant with respect to temperature. This is obviously not the case, but the differences are small enough to make it a suitable starting point. We now have two equations (3.10 and 3.11) with two unknown parameters ($\Delta T_s\left(t\right)$ and $\Delta\tilde{F}\left(t\right)$), so we can solve to obtain equations for $\Delta\tilde{F}(t)$ and $\Delta T_s(t)$

$$\Delta\tilde{F}(t) = \frac{\delta\left[\frac{\mathrm{d}M}{\mathrm{d}T}\right]\Delta\tilde{\Theta}\left(t\right) - \frac{\mathrm{d}M}{\mathrm{d}T}\delta\left[\Delta\tilde{\Theta}\left(t\right)\right]}{\frac{\mathrm{d}M}{\mathrm{d}T}\delta\left[M_0\right] - M_0\delta\left[\frac{\mathrm{d}M}{\mathrm{d}T}\right]} \tag{3.12}$$

$$\Delta T_s(t) = \frac{\delta\left[M_0\right]\Delta\tilde{\Theta}\left(t\right) - M_0\delta\left[\Delta\tilde{\Theta}\left(t\right)\right]}{\tilde{F}_0\frac{\mathrm{d}M}{\mathrm{d}T}\delta\left[M_0\right] - \tilde{F}_0M_0\delta\left[\frac{\mathrm{d}M}{\mathrm{d}T}\right]} \tag{3.13}$$

Due to the approximation $\delta[\Delta T_s(t)] = 0$, the results are similar to the earlier thermal difference scheme. However with these equations we can continue our analysis to come up with a better estimate of the $\delta[\Delta T_s(t)]$ term, and thereby improve the precision of our calculation.

The first guess, the naive interpretation of the MOKE-signal as the magnetization directly, neglecting $\Delta\tilde{F}(t)$ completely, is obviously an overestimate of the magnetization transient. The second guess (generalized thermal difference scheme) however will be an overestimate of the generalized Fresnel factors ($\tilde{F}(t)$), because of the fact that the changing heat-capacities are incorporated into the optical effects. So the true magnetization signal will be a curve lying in between these limits.

3.4 Iterative scheme

Getting closer to the true magnetization transient means making a better estimate of the $\delta[\Delta T_s(t)]$ term, which we have neglected so far. At this point it would seem straightforward to calculate $\delta[\Delta T_s(t)]$ from the data in figure 3.4, but these were calculated using equation 3.10, and, although we would probably get a little closer to the magnetization behavior, we would have no way of knowing how close.

A second approach might be to try to solve it iteratively, i.e. calculate $\Delta T_s(t)$ at two different ambient temperatures with the thermal difference scheme to estimate $\delta[\Delta T_s(t)]$. This however has the drawback that one then would need MOKE-measurements at three different temperatures, and every iteration would need another measurement at a different ambient temperature. So at this point the previously introduced S3TM (see section 2.3) can be used to *simulate* the spin-temperature.

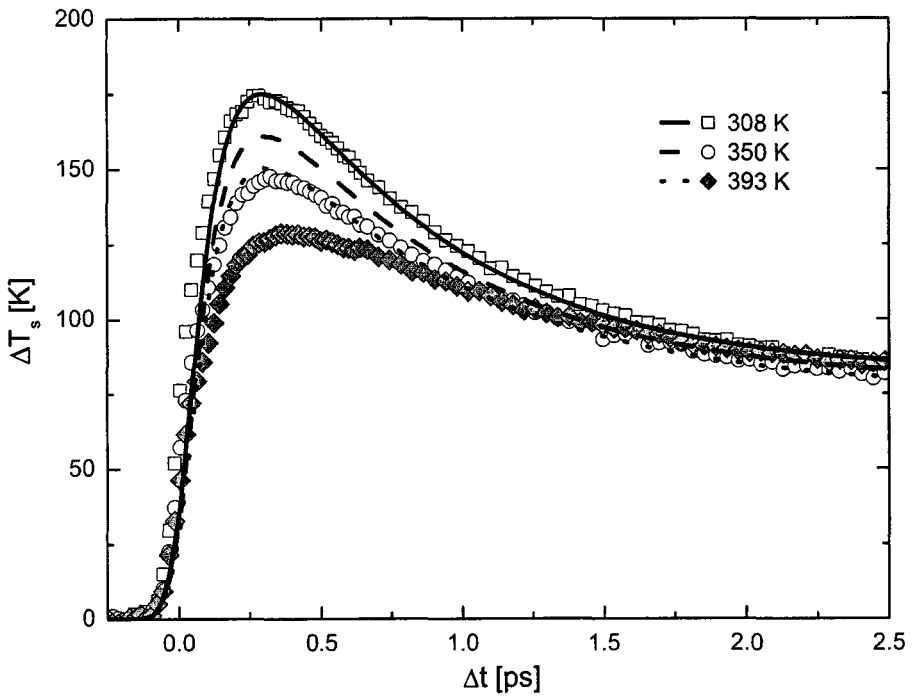

Figure 3.5: Spin-temperature transients from Fig. 3.4, the solid lines have been calculated using the simplified three temperature model. The parameters, $c_l = 2.8 \cdot 10^6$ J/m^3/K, $\gamma = 3.76 \cdot 10^3$ J/m^3/K, $g_{el} = 150 \cdot 10^{16}$ W/m^3/K and $\tau_{AI} = 100$ fs, are chosen to match the measurements at 308 K. Reproduced from ref.[2]

If the right parameters for the S3TM are chosen the curves in figure 3.4(c) can be reproduced; In figure 3.5 the parameters are chosen to fit the curve at 308 K. From measurements of the total heat-capacity, the electron ($c_e(T_e)$) and lattice (c_l) heat capacities can be calculated [2]. Actually, the precise value of the heat capacities is not that important as long as their ratio remains constant; because of the difficulty in estimating the portion of the laser energy that is deposited in the layer of interest. Thus the laser fluence or the total heat capacity can always be scaled to get the right temperature. The electron-lattice coupling constant g_{el} can be calculated using equation 2.13, which requires knowledge of τ_E. τ_E can be independently estimated from transient reflectivity measurements [2], and was reported to be in the range $0.4 - 1.3$ ps. τ_M is a completely free parameter which can be fitted to reproduce the spin temperature.

The S3TM is not able to fit all the data simultaneously; primarily the maxima of the curves at higher ambient temperature are estimated too high. In terms of the model this means an underestimation of electron heat-capacity, which is mainly responsible for the peak in the electron (and thus spin) temperature. However, from the ratio of the peak and equilibrium temperatures ($\Delta T_1, \Delta T_2$ in figure 2.4), the ratio of the heat capacities is known, and the total heat capacity can easily be measured. Thus this overestimation of the peak temperatures would seem to indicate a failure of the S3TM to describe the data.

Using the simplified three temperature model (S3TM) introduced in section 2.3, we can make an estimate of the $\delta[\Delta T_s(t)]$ term, assumed to be zero in equation (3.11). We do this by fitting the S3TM to the spin temperature at T_0, and use the temperature dependence of the model with these parameters to account for the transients at T_1, with which the $\delta[\Delta T_s(t)]$ is estimated. So now we solve equations (3.10) and (3.11) again for $\Delta\tilde{F}(t)$ and $\Delta T_s(t)$

$$\Delta\tilde{F}(t) = \frac{\delta\left[\frac{dM}{dT}\right]\Delta\tilde{\Theta}(t) - \frac{dM}{dT}\delta\left[\Delta\tilde{\Theta}(t)\right] + \tilde{F}_0\left(\frac{dM}{dT}\right)^2\delta[\Delta T_s(t)]}{\frac{dM}{dT}\delta[M_0] - M_0\delta\left[\frac{dM}{dT}\right]} \tag{3.14}$$

$$\Delta T_s(t) = \frac{\delta[M_0]\Delta\tilde{\Theta}(t) - M_0\delta\left[\Delta\tilde{\Theta}(t)\right] + \tilde{F}_0 M_0\frac{dM}{dT}\delta[\Delta T_s(t)]}{\tilde{F}_0\frac{dM}{dT}\delta[M_0] - \tilde{F}_0 M_0\delta\left[\frac{dM}{dT}\right]} \tag{3.15}$$

Of course, with the estimate of $\delta[\Delta T_s(t)]$ by the S3TM, we still have no way of knowing how close the solution is to the actual magnetization behavior. However, the estimation of the S3TM gives us a good method to iteratively try to come to a self-consistent solution. This iterative scheme would then work as displayed in figure 3.6; the first step is doing the MOKE-measurements at two different temperatures, calculating the spin temperature at T_0 using equation 3.10, and simulating the corresponding spin-temperature curves, using fitted values for the constants in the S3TM. The second step is calculating $\Delta\tilde{F}(t)$ and $\Delta T_s(t)$ using equations (3.14) and (3.15). Then the S3TM can be used to fit the newly calculated $T_s(t)$ to obtain a new value for τ_M. Using the parameters obtained from the original fit, with the new τ_M, a new spin-temperature at the elevated temperature can be simulated. At this point the circle is completed and new $\Delta\tilde{F}(t)$ and $\Delta T_s(t)$ can be calculated again.

3.5 Results & Discussion

Figure 3.7 shows a comparison of the spin temperature transients calculated with the different schemes presented before. $\Delta T_s^{(0)}$ represents the naive calculation of equation 3.10. $\Delta T_s^{(1)}$ is the spin temperature calculated using the thermal difference scheme (equation 3.13), and $\Delta T_s^{(2)}$ corresponds to the result of the first iteration of equation 3.15. The second and third order spin temperature maxima are 50% lower than the naive interpretation, which suggest that within the first picosecond approximately 50% of the effect is due to optical artifacts.

As expected, the first order calculation shows an overestimation of the spin-temperature, and the second order calculation shows an overestimation; the third order calculation produces a curve which give an intermediate result. Because of overestimation and underestimation respectively

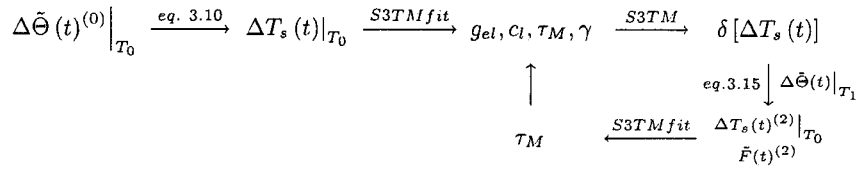

Figure 3.6: Iterative scheme to extract the spin-temperature from the MOKE-data. Using the measured data at two temperature and the known magnetization behavior with equation 3.10 the spin-temperature is calculated. Then the S3TM is fitted to this spin-temperature and a spin-temperature at the elevated temperature can be calculated using the fitted parameters, producing the $\delta[\Delta T_s(t)]$ term. Equations 3.15 and 3.14 are then used to calculate the next iteration ($\Delta T_s(t)^{(2)}\big|_{T_0}$ and $\Delta\tilde{F}(t)$). The scheme can then be continued by again fitting the S3TM to $\Delta T_s(t)^{(2)}\big|_{T_0}$.

of the first and second order curves, this seems to be a better approximation to the magnetization behavior. However, as mentioned before, we have no way of knowing how good this third order guess actually was, so we will continue with our iterative scheme for a few more steps to find out if this iterative scheme leads to a self-consistent solution.

The generalized Fresnel factors (see figure 3.7b) display a complementary behavior supporting the view presented by figure 3.7a.

The results of these calculations are displayed in figure 3.8. In subsequent iterations the characteristic demagnetization time increased until the solution became stable at a τ_M of approximately 840 fs. The heat capacities $c_l = 5.03 \cdot 10^6$ Jm^{-3}K^{-1} and $\gamma T_e = 2.08 \cdot 10^6$ Jm^{-3}K^{-1} and the electron-lattice coupling constant $g_{ep} = 269 \cdot 10^{20}$ Wm^{-3}K^{-1} have been kept constant. This is necessary in order to fix τ_E, which can be determined independently by time resolved reflectivity studies, and has been found to be around 0.6 ps in nickel films [2].

However, due to the poorness of the fit (see figure 3.9) this number is an exaggeration of the actual demagnetization time. Looking only at the maxima of the curves we can estimate that the real demagnetization time will be approximately 250 fs shorter than the fitted time.

The results of the iterations are shown in figure 3.10; only the first (open squares) and ninth (diamonds) iterations are shown. The view of figure 3.8 is confirmed by the shift of the maximum of the ninth iteration curve to longer delay time. Also a slight upward shift of the ninth iteration curve after 1 ps is visible. This is an unwanted result, because it would indicate a changing heat capacity. It is not clear where this effect originates from.

The changes in the spin temperature curves are also clearly visible in the optical effects transients (see figure 3.10b). Within the first picosecond the optical effects increase, after 1 ps the curve decays more rapidly. This is the exact complement of figure 3.10a. More important however, is the timescale of the optical effects as a whole. Because of the long duration, i.e. much longer than the electron thermalization time. We conjecture that this long timescale indicates that the optical effects originate from non-equilibrium pockets in the band structure of the material, created by bottlenecks in the thermalization process.

The general result of these calculations is that the demagnetization timescale is much longer than expected from the simple estimate. This is important because this opens up ways for microscopic explanations. In the naive interpretation ($\tau_M \approx 0.1$ ps) the explanation of the magneto optic Kerr effect seems to lie in effects taking place during electron thermalization. The new interpretation however allows for phonons to play a role in the process. This foreshadows the basis of the microscopic model (see chapter 4), in which a phonon-based mechanism is proposed to give a microscopic explanation of the ultra-fast demagnetization.

There are however a few drawbacks to this method; Firstly, while the formula's for the separation method are derived using only small temperature differences (pump powers), they are applied to the relatively large temperature differences of the experiments. This gives rise to

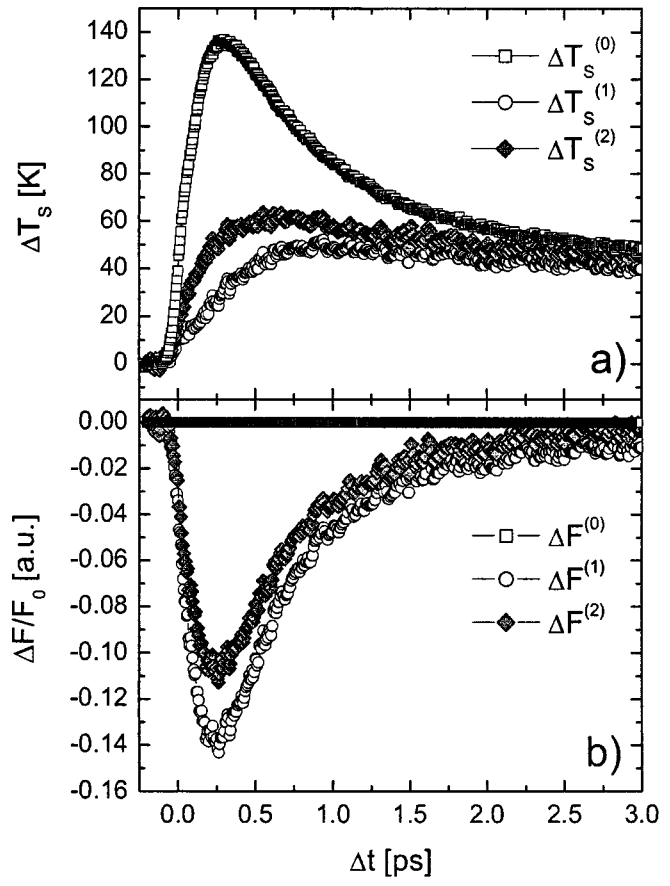

Figure 3.7: Calculated spin-temperature (a) and Fresnel factors (b) transients using the iterative scheme. The superscript numbers represent the "order" of the calculation; (0) The most naive interpretation of the MOKE-signal, computed using equation (3.10). (1) Thermal difference scheme equations (3.13). (2) 1st iteration of the iterative scheme.

extra non-linearities (magnetic) which are unaccounted for, due neglect of the non-linear terms in the equations.

Secondly, the calculation method is very sensitive to the starting values, i.e. the S3TM has to be fitted quite closely to the actual values in order to have $\Delta\tilde{F}$ converge to zero for long delay times.

Thirdly, and most importantly, the fitting of the successive curves with the S3TM is very poor, and it is very questionable if the convergent result is an easy interpretable quantity. In view of the poor fits, this result cannot be the genuine magnetization behavior, though it may still be a better estimate than the thermal difference scheme.

Also, another, experimental issue is causing the iterative scheme to fail at finding the genuine magnetization behavior. Due to the pump laser pulse having a spatial gaussian profile, the middle of the laser-spot is heated more than the edges, giving rise to different magnetic behavior. The probe laser pulse exhibits the same behavior, thus the middle of the laser-spot has even more influence on the measured result.

This overvaluation of the center of the laser spot can be compensated for [2], and the peak temperature at the laser spot can be calculated by

$$M_{probe} = M_0 + \frac{a}{2}T_0 + \frac{b}{3}T_0^2, \tag{3.16}$$

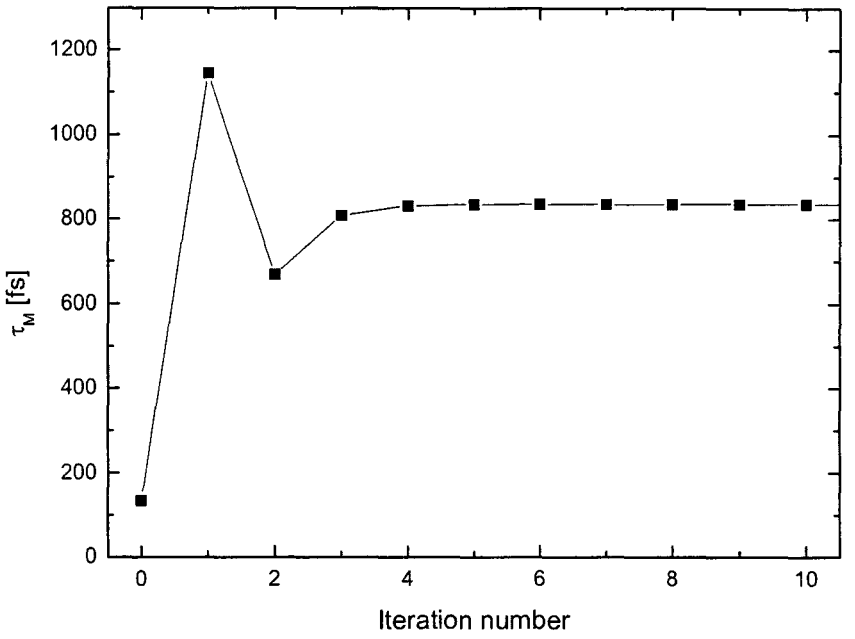

Figure 3.8: τ_M at subsequent iterations of the iterative scheme. After iteration 4 the solution becomes stable at a characteristic demagnetization time of approximately 839 fs.

with M_{probe} the probed magnetization, M_0 the equilibrium magnetization at ambient temperature, T_0 the temperature in the center of the laser spot, and a and b constants determined by the a quadratic fit to the equilibrium magnetization

$$M(T) = M_0 + aT + bT^2. \tag{3.17}$$

Thus, the spin temperature found by van Kampen through equation 3.16, is different from the spin temperature found with equation 3.10. Moreover, and most importantly, the ratio of the peak temperature and final temperature (ΔT_1 and ΔT_2 in figure 2.4) is not the same in both approaches. The transient reflectivity measurements of van Kampen (yielding a large number of the parameters used for fitting with the S3TM) are only applicable for fitting the spin temperatures calculated with equation 3.16, which accounts for the poor fitting displayed in figure 3.9.

This problem can be eliminated by performing experiments with very small pump powers. In these conditions the equilibrium magnetization versus temperature is approximately linear, yielding only terms linear in the spin temperature in equation 3.16.

3.6 Conclusions

In this chapter an iterative method was presented to calculate the true magnetic data from measurement data of the magneto optic Kerr effect. The iterative method is based on a thermal difference scheme proposed by van Kampen *et al.*[2]. The calculated magnetic curve shows a demagnetization time of approximately 0.8 ps; in comparison, if one naively interprets the MOKE-angle as a purely magnetic response, a demagnetization time of approximately 0.1 ps is found. For this faster timescale few microscopic mechanisms can be identified. However, more than doubling the timescale makes it more plausible to consider phonon based mechanisms as a candidate for ultra-fast demagnetization.

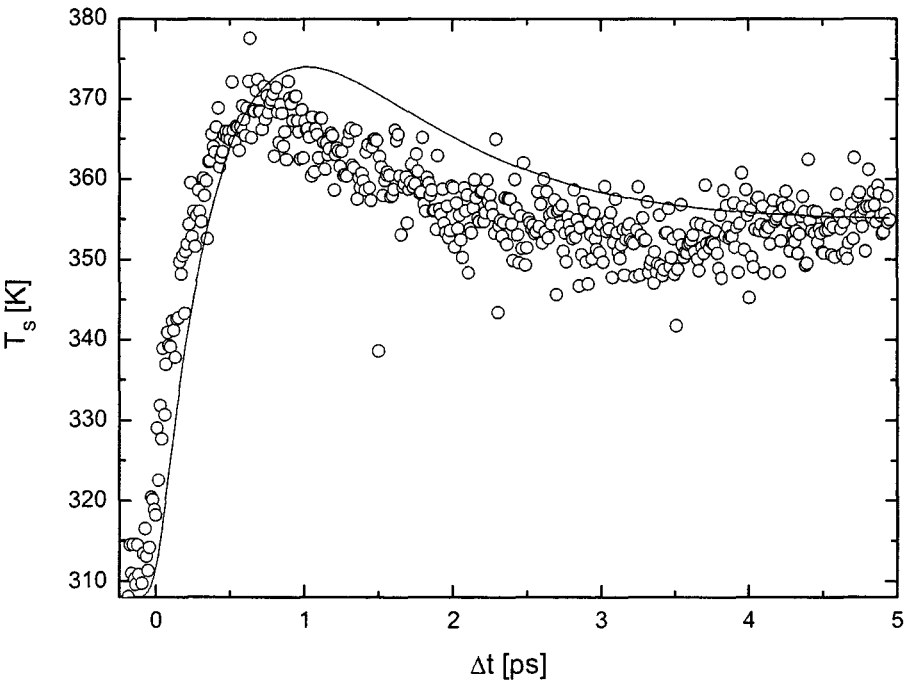

Figure 3.9: Spin temperature after the first iteration and the S3TM fitted curve; clearly visible is the fact that the S3TM is not able to fit the data. This remains a problem throughout all subsequent iterations.

The results of the calculation also confirm the expectation that optical effects such as bleaching and state-filling only contribute during the first picosecond. As to the doubts whether the magneto optic Kerr effect shows magnetism at all, it is shown that during the first 0.5 ps the measured MOKE-angle consist of more than 50% out of optical contributions.

Due to the poor fits with the S3TM the iterative thermal difference scheme does not yield the genuine magnetization dynamics. Though the results may still be better than the previous thermal difference scheme, there is no way of knowing this. The failure of the iterative scheme to extract the actual magnetization transient can be caused by two factors. First, non-linear factors in the equilibrium magnetization and in the pump induced expansion were neglected. Second, the S3TM may not be able to predict the right temperature dependent behavior of the magnetization dynamics.

The failure of the iterative method for the dataset by van Kampen, is caused by the non-linear magnetic contributions caused by the spatial profile of the pump and probe laser pulses. For much lower pump powers these non-linear magnetic contributions will be of little influence. Thus, it is recommended for future studies to perform experiments with low laser power, to verify the applicability of this method.

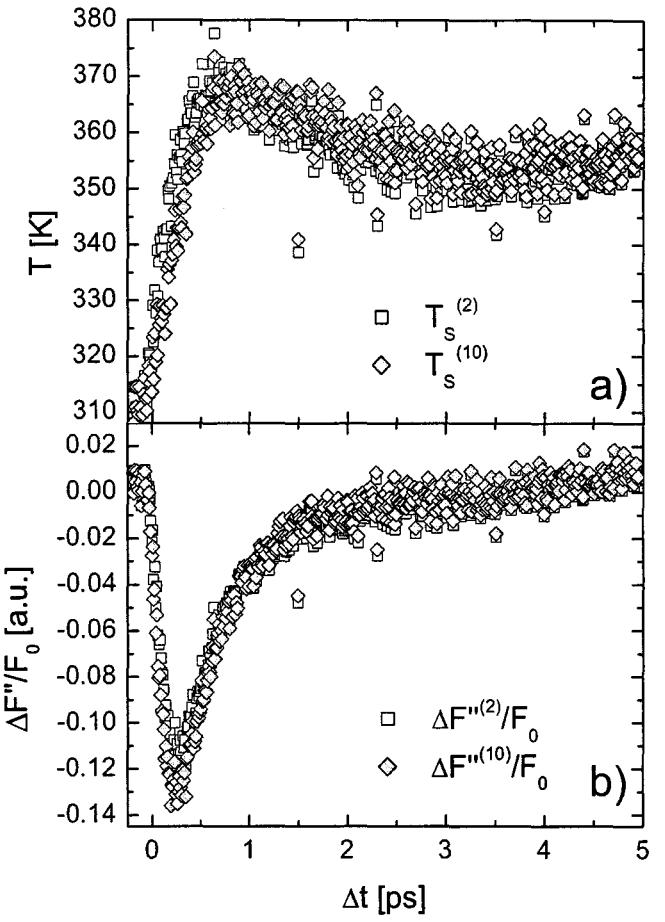

Figure 3.10: Comparison of the spin temperature and optical effects transients after the first and after nine iterations; The maximum of the spin temperature (a) is shifted to a longer timescale, supporting the view of figure 3.8. Also, after approximately 1 ps the curve of the ninth iteration shows a slightly higher end value. The ninth iteration Fresnel factor (b) transient shows an increase of the optical effects in the first picosecond and a decrease after 1 ps.

Chapter 4

Microscopic Model

Besides the problem of interpreting the magneto-optic Kerr effect, there is also the problem of explaining the ultra-fast magnetic response in the experiments of section 1.2. If we take a look at a typical experiment as made by van Kampen (see figure 3.1), and interpret this as a truly magnetic signal, we see a demagnetization of about 5% within 0.5 ps after the pump laser pulse has struck the sample. The timescale is so short that no broadly accepted theory exists, explaining the mechanisms behind this process. In this chapter we will explore some of the mechanisms and processes involved in such an ultra-fast demagnetization.

4.1 Mechanisms for demagnetization

In this section two models for ultra fast demagnetization will be discussed briefly (see section 4.1.1). Furthermore, a phonon based mechanism to describe the magnetization transients of the previous chapter will be investigated.

4.1.1 Other work

Hübner *et al.*[5] have developed a fully quantum-mechanical model in which demagnetization caused by the laser field and spin-orbit coupling is considered, and have shown a demagnetization within some tens of femtoseconds, neglecting any phonon contributions. Their model only shows a maximum demagnetization of about 50%. They attribute this saturation of the magnetic signal to bleaching effects, i.e. the depopulation of the optically accessible electronic energy levels, making it impossible to absorb any more photons, and thus saturating the demagnetization process.

Also, recently, Beaurepaire *et al.* [6] have suggested and measured that terahertz radiation emitted by the rapidly changing magnetic field might be another mechanism of getting rid of the magnetic moment. Although this process can indeed contribute to the transfer of orbital momentum, the effect is considered to be too small to be the sole mechanism responsible for the demagnetization process. It could, however, be a valuable addition.

4.1.2 Conservation of angular momentum

What are the mechanisms responsible for the decrease of the magnetization in a magnetic metal? First we write down some basic equations: the atomic magnetic moment is given by

$$\mathbf{M} = \mu_B \left(g\mathbf{S}_e + \mathbf{L}_e \right), \tag{4.1}$$

with $\mathbf{S}_e$ the spin-momentum of the electrons, $\mathbf{L}_e$ the orbital momentum of the electrons, and g the Landé-factor which is approximately 2 for electrons. Also we have to conserve angular momentum

$$\mathbf{J} = \mathbf{S}_e + \mathbf{L}_e + \mathbf{L}_{\hbar\omega} + \mathbf{L}_p, \tag{4.2}$$

with $\mathbf{L}_{\hbar\omega}$ the orbital momentum of the (pump) laser field, and $\mathbf{L}_p$ the orbital momentum of phonons. Mostly, in literature, the orbital momentum of phonons is neglected because of the large timescale involved in electron-phonon equilibration (full equilibration after approximately 3 ps). Also the orbital momentum of the laser field can easily be dismissed as the driving factor by a simple estimate. In a typical experiment on nickel [2] ($\approx 0.6\ \mu_B$ per atom) about 5% of the magnetic moment is quenched, which corresponds to a decrease of about $0.03\ \mu_B$ per atom. A typical laser fluence gives about 0.01 excitations per atom. If we consider the unrealistic case that we shoot a beam of linearly polarized light on the sample and the reflected beam is fully circularly polarized, then we would have decreased the magnetization by only $0.01\ \mu_B$ per atom. Considering the fact that the polarization of the reflected beam is actually only slightly changed, we can rule out a big role of the laser field in this process. Dropping these two contributions we are left with a reduced version of equation (4.2)

$$\mathbf{J} = \mathbf{S}_e + \mathbf{L}_e. \tag{4.3}$$

Thus, having to conserve angular momentum, the only way to reduce the magnetic moment is by transferring all the spin momentum of the electrons to orbital momentum. A simple estimate shows that this can maximally lead to a demagnetization of approximately 45% (see Example 1).

Example 1
Considering nickel with $0.6\ \mu_B$ per atom, and 90% of this is contributed by the $g\mathbf{S}_e$ term we find $S_e = 0.27$ and $L_e = 0.06$. With conservation of angular momentum we find $J = S_e + L_e = 0.33$. Decreasing the magnetic moment means converting all S_e into L_e, so $S_e = 0$ and $L_e = 0.33$. The total magnetic moment has thus been decreased from $0.6\ \mu_B$ per atom to $0.33\ \mu_B$ per atom, which is a decrease of 45%.

From experiment [7] it is found however that the magnetic moment can be quenched completely within a few picoseconds! Also, the Kerr signal is particularly sensitive to the orbital momentum contribution, and we would then see an increase in the Kerr signal, while exactly the opposite is found in experiment. So this means we might have been wrong in dismissing the orbital momentum contribution of phonons.

4.1.3 Proposed mechanism

Having ruled out a big role for the laser field with the estimate in section 4.1, it is clear that in order to achieve a full demagnetization (as shown in experiment [7]) phonons may have to be considered as a possible channel for orbital momentum interchange. Let us therefore consider a phonon-based mechanism for ultra-fast demagnetization. We propose an event in which the spin of the electron is flipped by collisions with phonons, similar to the Elliot-Yafet-type [8, 9] spin-orbit scattering (see section 4.3); the electron flips its spin and the phonon carries away the resulting orbital momentum. Hereby we assume the lattice to be a perfect sink for orbital momentum, giving rise to a finite turning of the sample as in the Einstein-de Haas experiment [10].

In this classic experiment (see figure 4.1) an iron rod is suspended from a thin wire in a coil. When a current is applied to the coil, a magnetic field is generated, and the rod starts turning. The explanation of this effect is that when the magnetic field magnetizes the iron rod, the spins of the electrons will be aligned along the magnetic field. For this to happen, under conservation of angular momentum, there will have to be a transfer of orbital momentum from the electrons to the lattice, resulting in a macroscopic rotation of the rod.

To make the argument of the inclusion of the phonons more plausible, we again make a simple estimate as we did before concerning the orbital momentum of the photons. Again, in the typical experiment of figure 3.1 a photon energy of about 2 eV is used to achieve a demagnetization of $0.03\ \mu_B$ per atom, with a laser fluence of 0.01 excitations per atom. This

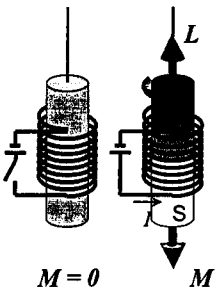

Figure 4.1: Einstein-de Haas experiment (1918). A demagnetized iron rod is suspended from a thin wire and placed in a coil. When a current is applied to the coil, a magnetic field is generated. The rod is also magnetized and starts turning.

means the lattice will have to absorb 0.02 eV per atom. Now considering the Debye-energy being about 40 meV in nickel, phonons will have an energy of 40 meV or less. Thus, there will have to be at least 0.5 electron-phonon event per atom to achieve this energy flux. So in order to reduce the magnetization by 0.03 μ_B per atom, we only need 1 spin-flip in every 15 electron-phonon events, which is not an absurd number considering the electron-phonon equilibration (τ_E) time is approximately 0.6 ps. (see Example 2)

Example 2
In a demagnetization experiment with a τ_E of 0.6 ps the lattice system is about 50% towards equilibrium, i.e. half the needed phonons are emitted after 0.6 ps. Considering 1 in every 15 e-p events is accompanied by a spin-flip, and there are 0.5 e-p events per atom needed in total (0.01 excitations per atom, phonon energy of 40 meV), we have approximately 0.017 μ_B per atom of flipped spins. However, in this calculation we have not considered the phonon absorptions! When the electrons and lattice are in equilibrium, the number of phonons emitted will equal the number of phonons absorbed. This means that during the equilibration process, the number of phonon absorptions will increase, and because of the 1 in 15 chance of spin-flip in these events, the demagnetization will surely have advanced more than 50% towards its equilibrium.

4.2 Processes

Having made the electron-phonon interaction with spin-flip an acceptable candidate for the ultra-fast demagnetization process, let us look at the processes and interactions that occur in a demagnetization experiment (see figure 4.2). First, as the pump-pulse strikes the sample, electrons will be excited to a depth of $h\nu$ below the Fermi-level. Because the pump beam is linearly polarized (i.e. equal amounts of left and right circularly polarized light), and the fact that the polarization state of the reflected beam is only slightly changed, these transitions will be mostly spin-conserving. Through electron-electron (e-e) collisions this excited state will thermalize (i.e. produce a Fermi-Dirac distribution). Following the argument of section 4.1 (angular momentum conservation) there will be very little spin-relaxation during these phases. The e-e interactions are a very efficient means of distributing the energy delivered by the pump-laser, and thermalization takes place within the first 100 fs. After only tens of femto-seconds the electron-distribution is close to equilibrium, and further changes in the electron distribution will be minor. At this time the electron-phonon (e-p) interactions become more important. Due to the small energy of the phonons there will be a large number of states near the Fermi-level with a large probability for e-p scattering. While the e-p interactions equilibrate the electron

and lattice systems, also the spin-system will equilibrate through the proposed mechanism of section 4.1.3.

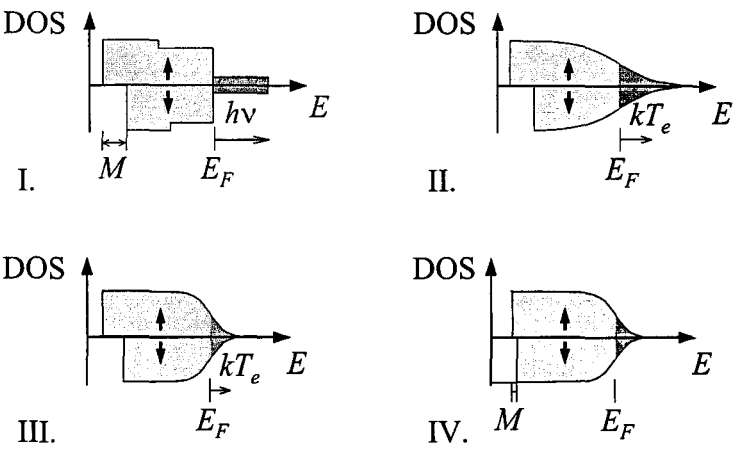

Figure 4.2: Schematic depiction of the evolution of the density of states in the case a ferromagnetic material is heated by a high power laser pulse. I. A spin imbalance in the density of states (DOS) gives rise to a net magnetic moment, the laser pulse creates excited electrons. II. Electron-electron scattering reforms a Fermi-Dirac distribution. III. Electron-phonon interactions equilibrate electrons and lattice. IV. Spin scattering processes decrease the magnetic moment M by creating a more balanced situation between spin-up and spin-down electrons. In this example the spin scattering process is shown to be slower than the electron-phonon equilibration timescale, contrary to experimental results.

The considered scattering processes in a ferromagnet are dipicted in figure 4.3; each of the processes can be assigned a probability, which corresponds to an inverse timescale. For the electron-thermalization a probability $K_{ee} \sim \tau_{th}^{-1}$ is assigned. For the electron-phonon events a similar constant is assigned. In the case of a non-magnetic metal, the probability of an e-p event is $K_{ep} \sim \tau_E^{-1}$. However, in presence of a spin-split band-structure a spin-flip probability α_{sf} (where sf stands for spin-flip) is introduced, which gives the ratio of spin-flip events to non-spin-flip events. The probability of non-spin-flip scattering is then $(1 - \alpha_{sf}) K_{ep}$ and the probability of spin-flip scattering is $\alpha_{sf} K_{ep} \sim \tau_M^{-1}$. α_{sf} ranges from 0 (no spin-flips) to 1 (every e-p event is a spin-flip). For realistic situations α_{sf} is expected to be less than 0.5. As was found in section 4.1.3, $\alpha_{sf} = \frac{1}{15}$ was sufficient to produce a demagnetization time smaller than the electron-phonon equilibration time.

4.3 Elliot-Yafet type Spin-Orbit scattering

Phonon mediated spin-flip scattering in metals is mainly due to the spin-orbit interaction as was discussed in section 4.1. The spin-orbit interaction couples the orbital and spin momentum of electrons, and it is due to the interaction of the electron's spin with the magnetic field that it sees because of the relative motion of the charge of the nucleus and of other electrons. Because of screening effects and the fact that outer electrons have larger orbits, the spin-orbit interaction will be stronger for the inner electrons. In 3d transition metals, like nickel, this is also of importance due to the fact that the 3d-orbitals, whose spin-split states give nickel its ferromagnetic behavior, are relatively close to the core.

The problem of an electron in a solid is usually treated as if the electron is moving in a perfect rigid lattice under a periodic potential. The Schrödinger equation is

$$\left[\left(\frac{\mathbf{p}^2}{2m}\right) + U(\mathbf{r})\right] \Psi = E\Psi \tag{4.4}$$

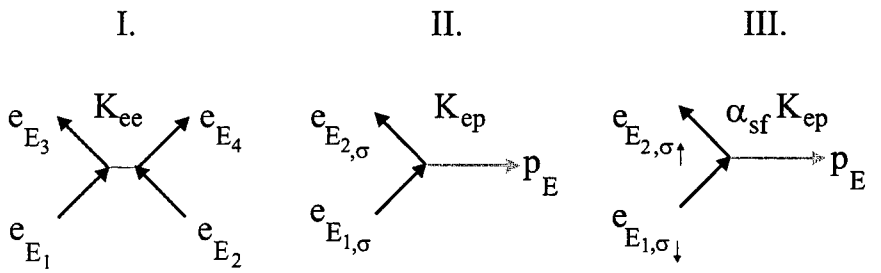

Figure 4.3: Schematic depiction of the scattering processes in a ferromagnetic material I. Electron-electron scattering: two electrons with energy E_1 and E_2 respectively collide and redistribute their energies. The probability of scattering is K_{ee}. II. Electron-phonon scattering: an electron of energy E_1 interacts with the lattice and emits or absorbs a phonon, changing its energy to $E_2 = E_1 \pm E_p$. The probability of interaction is K_{ep}. III. Electron-phonon scattering with spin-flip: an electron of energy E_1 interacts with the lattice, emitting or absorbing a phonon, en simultaneously flipping its spin. The resulting orbital momentum is carried away by the phonon. The probability of this process is $\alpha_{sf} K_{ep}$.

where $U(\mathbf{r})$ is the periodic lattice potential. Using periodic or Born-von Karman boundary conditions this leads to the well known Bloch functions

$$\Psi = u_k e^{i\mathbf{k}\cdot\mathbf{r}} \tag{4.5}$$

where u_k has the symmetry of the lattice. This can be expanded to include spin by writing

$$\Psi = \psi(\mathbf{r})\chi(\sigma), \tag{4.6}$$

with $\chi(\sigma)$ the spin wavefunction, and σ the spin of the electron. Because the spin operator $\mathbf{S}$ and the Hamiltonian commute, the wave functions can be written as a simple product of eigenfunctions. In ferromagnetic materials this picture is complicated by a previously neglected term in the Hamiltonian, the spin-spin interaction. In non-magnetic materials this term is of little importance due to the fact that the spin-spin interactions average to zero in a very short time as the result of rapid translational motion of the electrons.

For ferromagnetic materials, however, there will always be an average magnetic moment due to the spin-split electronic levels. The Schrödinger equation then becomes

$$[\mathcal{H}_0 + \mathcal{H}_s]\Psi = E\Psi, \tag{4.7}$$

where $\mathcal{H}_0$ is the Hamiltonian of equation (4.4) i.e. the spatial dependence, and $\mathcal{H}_s$ is the spin contribution. In general, because of the vast amount of electrons in a solid the Schrödinger equation including spin-spin interactions is not solvable. However, if we treat these in a mean field approximation, the spin Hamiltonian is independent of spatial coördinates, and we can again write Ψ as in equation (4.6). Furthermore, this has not changed the form of equation (4.4) and the Bloch functions will therefore remain valid wave functions although with different functions u_k.

If we also include spin-orbit (SO) coupling, equation (4.7) becomes

$$[\mathcal{H}_0 + \mathcal{H}_s + \mathcal{H}_{so}]\Psi = E\Psi, \tag{4.8}$$

$$\mathcal{H}_{so} = \left(\frac{e^2}{4\pi\epsilon_0}\right)\frac{1}{m^2c^2r^3}\mathbf{S}\cdot\mathbf{L}, \tag{4.9}$$

with e the electronic charge, ϵ_0 the dielectric constant, m the mass of the electron, c the speed of light in vacuum, r the radius of the orbit around the nucleus, $\mathbf{S}$ the spin momentum operator, and $\mathbf{L}$ the orbital momentum operator. Spin-orbit coupling mixes spatial and spin dependencies

in the Hamiltonian, and **S** will in general not commute with $\mathcal{H} = \mathcal{H}_0 + \mathcal{H}_s + \mathcal{H}_{so}$, which means spin is no longer a good quantum number. Because there is a term in the spin operator in the Hamiltonian, the eigenfunctions will now be linear combinations of different spin functions [8]

$$\Psi^{\uparrow}_{\mathbf{k}n}(\mathbf{r}) = [a_{\mathbf{k}n}(\mathbf{r})\,|\uparrow\rangle + b_{\mathbf{k}n}(\mathbf{r})\,|\downarrow\rangle]\,e^{i\mathbf{k}\cdot\mathbf{r}}, \tag{4.10}$$

$$\Psi^{\downarrow}_{\mathbf{k}n}(\mathbf{r}) = [a^{*}_{-\mathbf{k}n}(\mathbf{r})\,|\downarrow\rangle - b^{*}_{-\mathbf{k}n}(\mathbf{r})\,|\uparrow\rangle]\,e^{i\mathbf{k}\cdot\mathbf{r}}, \tag{4.11}$$

with $\mathbf{k}$ the lattice momentum or wave number, and n the band index, and $a_{\mathbf{k}n}(\mathbf{r})$ and $b_{\mathbf{k}n}(\mathbf{r})$ complex periodic functions with the periodicity of the lattice, similar to the u_k functions. In non-ferromagnetic materials, and in absence of an external magnetic field both states have the same energy, as follows from space and time inversion. However, due to the spin-split band structure of a ferromagnetic metal, these states are generally non-degenerate, and belong to different bands.

The states $\Psi^{\uparrow}_{\mathbf{k}n}$ and $\Psi^{\downarrow}_{\mathbf{k}'n'}$ are chosen to represent electrons with spins polarized along the z direction [9]:

$$\left(\Psi^{\downarrow}_{\mathbf{k}'n'} \mid \hat{S}_z \mid \Psi^{\downarrow}_{\mathbf{k}'n'}\right) = -\left(\Psi^{\uparrow}_{\mathbf{k}n} \mid \hat{S}_z \mid \Psi^{\uparrow}_{\mathbf{k}n}\right) = -\frac{\hbar}{2}\left(|a_{\mathbf{k}n}|^2 - |b_{\mathbf{k}n}|^2\right) \approx -\frac{\hbar}{2} \tag{4.12}$$

This means that $a_{\mathbf{k}n}(\mathbf{r})$ have values close to one, while $b_{\mathbf{k}n}(\mathbf{r})$ are much smaller, decreasing with the strength of the spin-orbit coupling. Due to this mixing of spin-up and spin-down functions in the electron wave functions, impurity or phonon scattering can induce transitions between $\Psi^{\uparrow}_{\mathbf{k}n}$ and $\Psi^{\downarrow}_{\mathbf{k}'n'}$, leading to spin relaxation. Under some simplifying assumptions an estimate of the spin relaxation time T_1 can be obtained [11].

$$\frac{1}{T_1} \approx \frac{4\langle b^2\rangle}{\tau}, \tag{4.13}$$

where $\langle b^2\rangle$ is the Fermi surface average of

$$|\,b_{\mathbf{k}n}\,|^2 = \sum_{\mathbf{G}} |\,b_{\mathbf{k}n}(\mathbf{G})\,|^2, \tag{4.14}$$

with **G** reciprocal lattice vectors. The Elliot-Yafet spin-flip probability (α_{EY}) can then be defined as

$$\alpha_{EY} = \frac{\tau}{T_1} \cong 4\langle b^2\rangle. \tag{4.15}$$

Spin-orbit interaction can be treated as a perturbation in most situations, which makes the average spin-mixing parameter $\langle b^2\rangle$ much smaller than one and thus $1/T_1 \ll 1/\tau$. The spin-mixing parameters $|\,b_{\mathbf{k}n}\,|^2$ can have a broad range of values, depending on the $\mathbf{k}$-value in the Brillouin zone.

Monod and Beuneu [12] have made conduction electron spin resonance (CESR) measurements for various metals. The CESR line-widths are a measure of the spin-scattering time. From these measurements a table of spin-flip scattering probabilities could be compiled [13].

The results, as listed in table 4.1, show a few remarkable values; first the extremely high spin-flip probability for Au, and second the fact that two neighboring metals in the periodic system (Na and Al) have such different spin-flip probabilities (a difference of almost 2 orders of magnitude). Although the high spin-flip probability of gold seems anomalous at first, a logarithmic plot of the spin-flip probability as a function of atom number, Z, (see figure 4.4) shows Au nicely fitting in with the alkali and noble metals. However, Aluminium clearly deviates from the "main" group, and more importantly from its next-neighbor in the periodic system, Sodium. At first glance we would not expect them to be so different, especially considering the spin-orbit interaction is proportional to Z^4. Because of their atomic similarity we expect the higher scattering probability in Aluminium to be the result of specific properties of the band structure.

Table 4.1: Experimental spin-flip probability (α_{EY}) for various metals, reproduced from ref [13]

Metal	Z	α_{EY}.
Na	11	$9.0 \cdot 10^{-6}$
K	19	$0.10 \cdot 10^{-3}$
Rb	37	$1.60 \cdot 10^{-3}$
Cs	55	$17.0 \cdot 10^{-3}$
Cu	29	$1.05 \cdot 10^{-3}$
Ag	47	$2.80 \cdot 10^{-3}$
Au	79	0.22
Al	13	$0.53 \cdot 10^{-3}$

Consider a band-structure computed without spin-orbit interaction, if two bands are separated by Δ then the two-band approximation for spin-orbit coupling gives for the Hamiltonian

$$\mathcal{H} = \begin{pmatrix} 0 & V_{so} \\ V_{so} & \Delta \end{pmatrix}, \tag{4.16}$$

with V_{so} the effective spin-orbit potential, presumed to be real, and Δ the interband separation. Seeking the eigenvalues of $\mathcal{H}\Psi = E\Psi$, we find the determinant

$$\begin{vmatrix} -E & V_{so} \\ V_{so} & \Delta - E \end{vmatrix} = 0. \tag{4.17}$$

This gives for E

$$E = \frac{\Delta \pm \sqrt{\Delta^2 + 4V_{so}^2}}{2}. \tag{4.18}$$

Then the eigenfunctions can be found, this yields for $\mid b_{\mathbf{k}n} \mid^2$

$$\mid b_{\mathbf{k}n} \mid^2 \approx \frac{1 - \frac{\Delta}{\sqrt{\Delta^2+4V_{so}^2}}}{2}. \tag{4.19}$$

Three different cases can be distinguished:

1. In a general point (near Γ) the band separation is of order E_F, the Fermi energy, so $\Delta \gg V_{so}$ and $\mid b_{\mathbf{k}n} \mid^2 \approx (V_{so}/E_F)^2$.

2. The state is close to a Brillouin zone plane that cuts $\mathbf{G}$ by half, the band separation is $\approx 2V_{\mathbf{G}}$, with $V_{\mathbf{G}}$ the $\mathbf{G}th$ Fourier coefficient of the non-spin part of the lattice potential. Since $V_{\mathbf{G}}$ is typically much larger than V_{so}, $\mid b_{\mathbf{k}n} \mid^2 \approx (V_{so}/2V_{\mathbf{G}})^2$, which can be a few orders larger than case 1.

3. The spin-orbit interaction can lift the degeneracy of two or more bands. The mixing of the spins is complete and $\mid b_{\mathbf{k}n} \mid^2 \approx \mid a_{\mathbf{k}n} \mid^2 \approx 0.5$. These states are not covered by the Elliot-Yafet theory [9], however Fabian and Das Sarma [11] show that these states are statistically relevant. The Fermi-surface average of $\langle b^2 \rangle$ is almost entirely determined by cases 2 and 3, and both cases contribute equally.

To illustrate how the band structure affects the spin relaxation, Fabian and Das Sarma [11] have made a pseudopotential calculation for aluminium, where all three cases occur. Figure 4.5

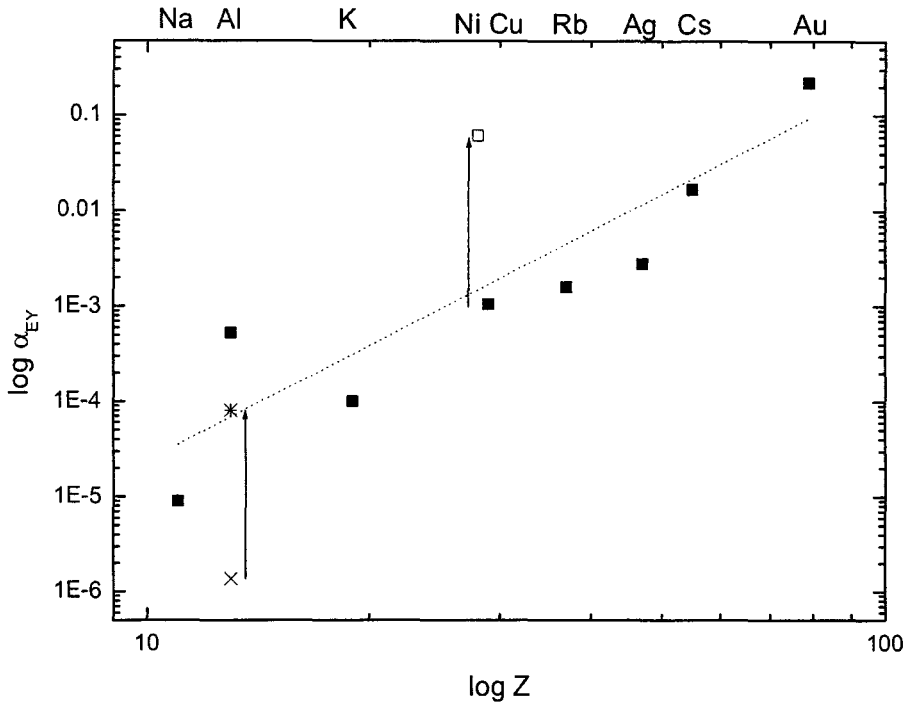

Figure 4.4: Spin-flip probabilities (α_{EY}) vs. atom number Z for various metals; the dotted line is a Z^4 fit (spin-orbit coupling) to the data of table 4.1. Clearly visible is Aluminium deviating from the "main" group of alkali and noble metals . For aluminium two further data points are added. The star indicates the spin-flip probability of aluminium calculated with the hot-spot theory, and the cross indicates theoretical mono-valent aluminium. Moreover, the projected α_{EY} for nickel is indicated by the open square.

shows the distribution ρ of the Fermi surface average of the spin-mixing parameters $\mid b_{\mathbf{k}n} \mid^2$. Also, in figure 4.6, the spin-flip probabilities are shown in a stereogram of the Fermi momentum directions. The colors violet, blue, green, yellow and red indicate successive increases of b^2. Each successive color indicates an increases of one order of magnitude from 10^{-5} - 10^{-4} for violet, up to 10^{-1} - 1 for red.

The span of the spin-mixing parameters is enormous (almost seven orders of magnitude). Most of the states have $\mid b_{\mathbf{k}n} \mid^2$ below 10^{-5}, these are the generic points of case 1. When the Fermi surface approaches the Brillouin zone planes (violet in figure 4.6), the values jump to 10^{-5} - 10^{-4}. The largest values $\mid b_{\mathbf{k}n} \mid^2$ are found near the accidental degeneracy points, so called "hot spots" (red spots in figure 4.6). At these points the bands are degenerate when no spin-orbit interaction is present. Spin-orbit coupling completely mixes the spin states as in case 3. The role of the band-structure becomes even more evident from the dashed curve in figure 4.5 for theoretical monovalent aluminium. In this case the Fermi surface does not cross a Brillouin zone plane, and no degenerate points of type 3 are present. The distribution of the spin-mixing parameters is much narrower and the Fermi surface average is $\langle b^2 \rangle \approx 3.4 \cdot 10^{-7}$, which leads to a spin-flip probability of approximately $1.4 \cdot 10^{-6}$.

When considering the values found with this theory in figure 4.4, it is evident that the hot-spot theory cannot fully explain the measured spin-flip probabilities. However, comparing the values found for mono-valent (cross) and tri-valent (star) aluminium, we find the enormous (almost 2 decades) influence of the bandstructure on the spin-flip probability.

Considering the bandstructure of Aluminium (see figure 4.7(a)), the spin scattering hot-

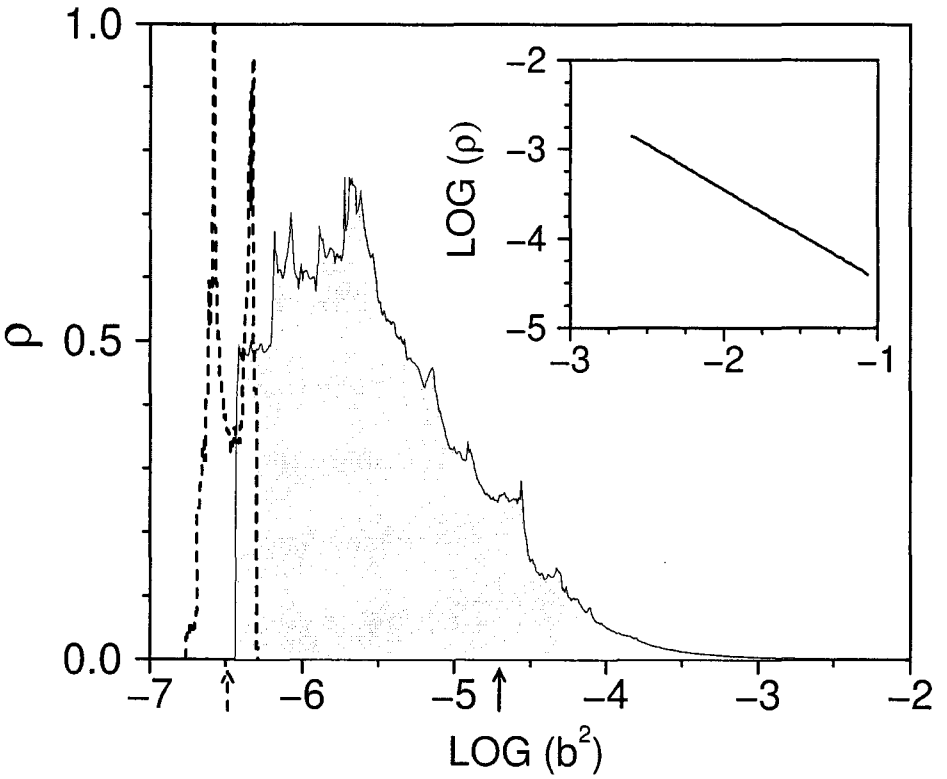

Figure 4.5: Calculated distribution ρ of the spin-mixing parameters $\mid b_{kn} \mid^2$ for aluminium. the average is indicated by a solid arrow. The linear tail of the distribution (contributions from states 3 are shown in the inset. The dashed line shows what the distribution would be if aluminium were monovalent. Reproduced from ref. [11].

spots can easily be found, namely the (near)-degenerate bands near the Fermi-level. If we now compare the band-structures of Copper and Nickel (see figures 4.7(b) and 4.7(c)), we see that nickel has a greater number of (near)-degeneracies, band crossings and bands lying very close to each other near the Fermi level than copper.

Although no theory of EY-scattering in ferromagnetic materials is available at present, we conjecture that because every degeneracy, band crossing and close-lying bands near the Fermi-level will enhance the spin scattering probability, nickel may have a significantly higher spin scattering probability than copper. A similar enhancement as for aluminium would make a spin scattering probability of the order of 0.1 realistic. Nevertheless, serious calculations will be needed to confirm this conjecture.

Experimentally this issue could also be resolved by measurement of the spin relaxation time, T_1. At this time we are not aware of any measurements of this type having been done for nickel.

4.4 Simple model

The previously introduced macroscopic simplified three temperature model is flawed in the sense that it is purely phenomenological. Although it can be fitted to the measurements, the model does not yield any physical understanding, nor has it any predictive power. Here a simple microscopic model is introduced that describes interactions among electron-, lattice- and spin-systems, in the simplest way possible, using the results of the analysis of sections 4.1 and 4.3.

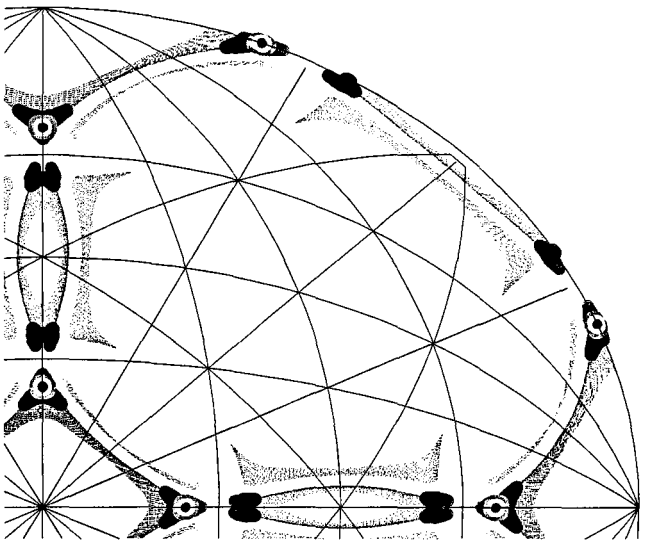

Figure 4.6: Stereogram of the Fermi momentum directions in aluminium, showing the spin-flip hot spots (in an extended zone scheme). White regions: $\mid b_{\mathbf{k}n} \mid^2 < 10^{-5}$. Via violet, blue, green, yellow and red ($10^{-1} < \mid b_{\mathbf{k}} \mid^2 < 1$), the calculated spin-flip rates increase in steps of one order of magnitude. Reproduced from ref. [11].

4.4.1 Model sub-systems

Electron system

The electrons are treated as a Fermi sea of spin-less particles, obeying Fermi-Dirac statistics. In equilibrium the occupation of electronic states is described by the Fermi-Dirac distribution

$$n(E) = \frac{1}{e^{\frac{E-E_F}{k_B T_e}} + 1}, \tag{4.20}$$

where E is the energy of a particular level, k_B is Boltzmann's constant, and T_e is the electron temperature. The number of electrons on a single level per atom $N(E)$ is then given by

$$N_e(E) = D_e(E)\, n(E). \tag{4.21}$$

As a severe approximation a constant Density of States ($D_e(E) = D_e$) is assumed for an energy range of 2 eV around the Fermi-level. We emphasize that this is a very crude approximation for ferromagnetic nickel. Furthermore, the wave vector of the electrons is not kept track of, which is the so called random $\vec{k}$ approximation.

Lattice system

The lattice system consists of a system of coupled oscillators (phonons), obeying Bose-Einstein statistics. In equilibrium the number of phonons per energy level is given by the Bose-Einstein distribution

$$n_p(E_p) = \frac{1}{e^{\frac{E_p}{k_B T_l}} - 1}, \tag{4.22}$$

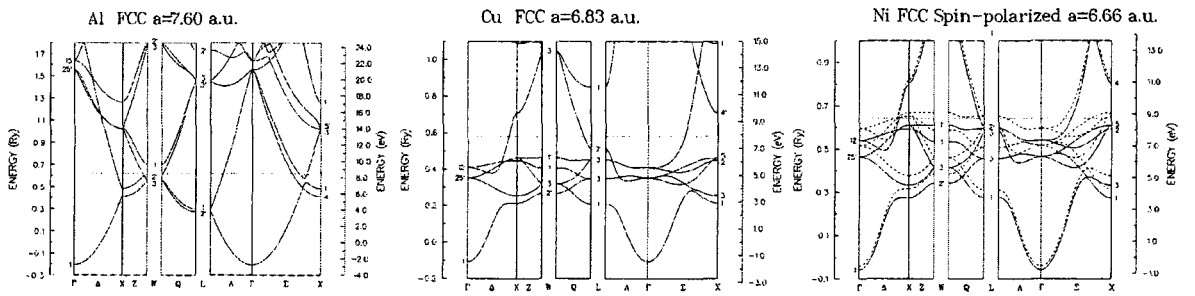

(a) Bandstructure of aluminium (b) Bandstructure of copper (c) Bandstructure of nickel

Figure 4.7: Calculated bandstructures of aluminium, copper and nickel. The Fermi-level is indicated by the dotted line. The spin scattering hot-spots are clearly visible in the bandstructures of aluminium and nickel as the (near) degeneracies close to the Fermi-level. Copper has a low spin scattering probability because of the very smooth behavior near the Fermi-level, with its d-bands approximately 2 eV below the Fermi-level.

with T_l the lattice temperature, and E_p the phonon energy. The number of scattering phonon modes per atom, $N_p(E_p)$ is given by

$$N_p(E_p) = D_p(E_p)\, n_p(E_p), \tag{4.23}$$

with $D_p(E_p)$ the density of modes.

The lattice is considered to continuously remain in internal equilibrium, i.e. we assume infinitely fast phonon-phonon interactions. In the Debye approximation the phonon energy, E_p, can range from zero up to the Debye-energy, which is approximately 36 meV for nickel.

Spin system

The spin system consists of a two level system with the lower level representing spin-up electrons and the upper level representing spin-down electrons, obeying Boltzmann statistics (see figure 4.8). All spins are chosen to be aligned to the z-direction. At $T = 0$ K all spins are aligned up, and the average spin per atom $s = 1/2$. The number of spins per atom in a particular level can be calculated by

$$n_{\sigma\uparrow} = D_m\left(\frac{1}{2} + s\right), \tag{4.24}$$

$$n_{\sigma\downarrow} = D_m\left(\frac{1}{2} - s\right), \tag{4.25}$$

where $n_{\sigma\uparrow(\downarrow)}$ is the number of spins in the lower (upper) level, and D_m the density of spins per atom, which is 0.6 μ_B per atom for nickel [3].

The energy difference or exchange splitting between spin-up and spin-down levels is chosen to be constant in the most simple model. In a refined model the exchange splitting will be made dependent on the average field induced by the spin-imbalance as in the Weiss model for magnetism.

4.4.2 Dynamics

Whereas in the S3TM the interactions among the three systems are modelled phenomenologically, the channels of energy exchange are now considered on a microscopic scale, identifying a mechanism for each interaction. Four interactions are considered (see figure 4.3), laser excitation, electron-electron (e-e) scattering, electron-phonon (e-p) scattering, electron-phonon with spin-flip (e-m) scattering.

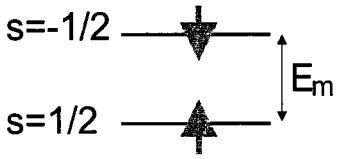

Figure 4.8: Magnetic two level (magnon) system. The spin-state of the levels are indicated by the gray solid arrows, and the energy difference or exchange splitting is E_m. Also indicated is the average spin, s, when all the spins are on the same energy level.

Direct interactions between lattice and spin system (phonon-magnon) scattering are considered to be too slow to contribute to the demagnetization effect, and thus excluded. For simplicity phonon-phonon interactions are chosen infinitely fast, i.e. the lattice system always stays in internal equilibrium, avoiding all problems with changing heat capacity.

Boltzmann equations

The dynamics of the microscopic model is described by so called Boltzmann equations. These rate equations count the probabilities of transitions of electrons from one level to another. Because of the vast number of electrons and therefore occupied levels (Pauli principle), summing over all levels becomes an integral. In general, a Boltzmann equation describing the interaction of electrons with a (quasi)particle x takes the form

$$\frac{\mathrm{d}n(E)}{\mathrm{d}t} = K_{ex} \int [-n(E) \cdot n_{x,-} \cdot [1 - n(E + E_x)] - n(E) \cdot n_{x,+} \cdot [1 - n(E - E_x)] + [1 - n(E)] \cdot n_{x,-} \cdot n(E - E_x) + [1 - n(E)] \cdot n_{x,+} \cdot n(E + E_x)] \, \mathrm{d}E, \quad (4.26)$$

with K_{ex} the electron-particle scattering probability, $n_{x,-}$ the particle annihilation (absorption) probability, $n_{x,+}$ the particle creation (emission) probability, and E_x the energy of the particle. In figure 4.9 a clarification of the different terms in equation 4.26 can be found.

For instance, consider the first term in this equation, $(-n(E) \cdot n_{x,-} \cdot [1 - n(E + E_x)])$. This term describes an event in which an electron in the state with energy E collides with a particle. In the collision the particle is annihilated, transferring its energy to the electron. Thus the electron jumps to a state with energy $E + E_x$.

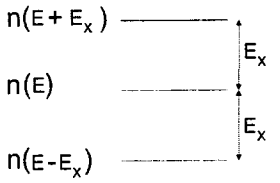

Figure 4.9: Electronic levels with a spacing of an arbitrary energy E_x. In equilibrium the occupations of the levels are given by the Fermi-Dirac distribution. The transitions from one level to another will be given by the electron distribution of the different levels and the number of available (quasi)particles x.

Laser excitation

At $t = 0$ the laser (pump) pulse initiates the demagnetization, electrons are excited from states below the Fermi-level to a depth of maximally $h\nu$. We have used two different implementations of this excitation (see figure 4.10).

a. "Smear"-excitation; the band-structure has lots of optically accessible states, so all the electrons within the $h\nu$ energy band around the Fermi-level have roughly the same chance

to get excited above the Fermi-level (see figure 4.10(a)). The excitation probability will be almost completely determined by the electron density

$$\frac{\mathrm{d}n(E_i)}{\mathrm{d}t} \propto n(E_i)\left[1 - n(E_i + h\nu)\right] \tag{4.27}$$

b. Band-excitation; some transitions in the band-structure are optically favored, e.g. the interband transition from the majority spin d-band to the sp-band in nickel, when the laser energy is tuned close to interband transition threshold. This gives rise to a completely different excitation profile (see figure 4.10(b)). In this case the probability of laser excitation is non-zero only in a narrow band around the laser energy. Also, if the laser-energy is high enough this type of laser excitation can lead to bleaching, setting an upper boundary on the quantity of energy which can be deposited in the electron system.

We found, however, that thermalization, electron-phonon equilibration, and demagnetization were only marginally influenced by the excitation scheme. This is due to the efficiency of the electron-electron scattering (next section), which ensures that the electron distributions of both excitation schemes will only differ significantly during the first few femtoseconds after laser excitation.

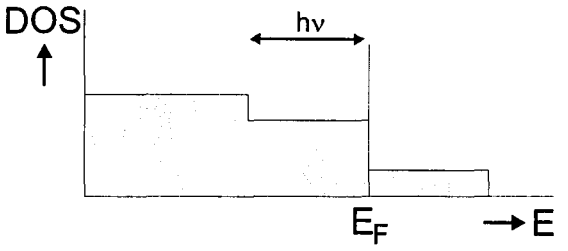

(a) "Smear"-excitation

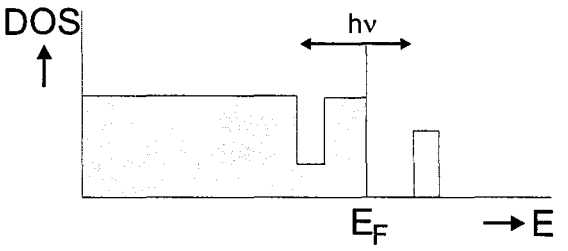

(b) Band-excitation

Figure 4.10: Two possible schemes for laser excitation in a metal. (a) "Smear"-excitation; the band-structure contains a lot of optically accessible states, so every state within an energy band equal to the laser energy below the Fermi-level has roughly the same chance for excitation (b) Band-excitation; some transitions are optically favored, and only these states have a non-zero probability for laser excitation.

Electron-electron scattering

The electron system is internally equilibrated by electron-electron scattering, which can be described by a Boltzmann equation

$$\begin{aligned}\frac{\mathrm{d}n_1}{\mathrm{d}t} = {} & K_{ee}D_e^3 \int\int\int \left[(1-n_1)(1-n_2)\cdot n_3 \cdot n_4 - \right. \\ & \left. n_1 \cdot n_2 \cdot (1-n_3)(1-n_4)\right] \delta(E_1 + E_2 - E_3 - E_4)\,\mathrm{d}E_2\mathrm{d}E_3\mathrm{d}E_4,\end{aligned} \tag{4.28}$$

with $n_i \equiv n(E_i)$ the value of the Fermi-Dirac distribution at energy E_i, K_{ee} the e-e scattering constant, and D_e the density of states. The density of states appears cubic in this equation, because every integration is over every electron on a certain energy level. However, on the left side the number of electrons also appears, so one power of D_e is eliminated.

The e-e scattering constant can be derived from the lifetime of excited electrons above the Fermi-level. From Fermi-liquid theory it is known that the characteristic decay time (τ_{ee}) is [14]

$$\tau_{ee}(E) = \frac{E_F^2}{K_{ee}(E - E_F)^2}. \tag{4.29}$$

From comparison with data from [14], E_F^2/K_{ee} for nickel was estimated to be 3 fs eV^2 [2].

Electron-phonon scattering

Electron-phonon scattering is the mechanism that equilibrates the electron and lattice systems. In terms of our model an electron with energy E_i interacts with the lattice, and emits a phonon of energy $\hbar\omega_p$, reducing its energy to $E_i - \hbar\omega_p$. For simplicity only one scattering phonon mode is chosen.

The electron-phonon interaction probability K_{ep} is proportional to the wave vector of the phonon ω_p [15].

$$K_{ep} = C\frac{\omega_p}{\rho V c^2}, \tag{4.30}$$

with ρ the specific mass, V the lattice volume, c the effective sound velocity, and the constant C is the square of a sort of mean potential energy of the scattering Bloch electron. This means that the phonons at the Debye-energy have the highest probability of interacting with electrons. Therefore only interactions with phonons of energy $\hbar\omega_p = k_B\Theta_D$, with Θ_D the Debye-temperature, are considered. The electron-phonon mechanism is described by the Boltzmann equation

$$\begin{aligned}\frac{\mathrm{d}n_E}{\mathrm{d}t} = \; & (1-\alpha_{sf})\; K_{ep}\; D_e\; D_p \\ & (-\, n_p\;\; n_E\left[1 - n_{E+E_p}\right] - (n_p+1)\, n_E\left[1 - n_{E-E_p}\right] + \\ & n_p\; n_{E-E_p}\left[1 - n_E\right] + (n_p+1)\, n_{E+E_p}\left[1 - n_E\right]),\end{aligned} \tag{4.31}$$

where $(1 - \alpha_{EY})$ is the probability of non-spin-flip scattering, and $n_E \equiv n(E)$, $E_p \equiv \hbar\omega_p$, and D_p the density of phonon modes per atom. The density of states appears linear in this equation, because every n_E term introduces a D_e, but one is compensated on the left side of the equation. The $(n_p + 1)$ terms are phonon emission terms (it is always possible to emit a phonon), and the n_p terms are phonon absorption terms (there has to be a phonon in order to absorb it). This equation can also be restated to give the change in the number of phonons per atom $\dot{n_p}$

$$\frac{\mathrm{d}n_p}{\mathrm{d}t} = (1-\alpha_{sf})\; K_{ep}\; D_e^2 \int \left[(n_p+1)\, n_E\left(1 - n_{E-E_p}\right) - n_p\; n_E\left(1 - n_{E+E_p}\right)\right] \mathrm{d}E. \tag{4.32}$$

Here the density of states D_e is not compensated, and the density of phonon modes disappears due to a compensating term on the left side.

Electron-phonon scattering with spin-flip

The mechanism that equilibrates both electron system and lattice system to the spin system is the electron-phonon interactions with spin-flip (e-m). To conserve angular momentum in this process the lattice is assumed to be a perfect sink for orbital momentum, giving rise to a finite rotation of the sample as in the Einstein-de Haas experiment [10]. This mechanism is very similar to the e-p interaction; an electron collides with an atom emitting (absorbing) a phonon

and flipping its spin. In this manner the electron reduces (increases) its energy by $E_p \pm E_m$, with E_m the energy difference of a spin-flip, which is equal to $g\mu H_{ex}$, with H_{ex} the molecular or Weiss field. In the most simple implementation of the model the average field H_{ex} and thus the energy difference is kept constant. In a more sophisticated model (see section 4.6) the energy difference or exchange splitting is made dependent on the average field. This mechanism can also be described by a Boltzmann equation

$$\begin{aligned}\frac{\mathrm{d}n_E}{\mathrm{d}t} = {} & \alpha_{sf}\ K_{ep}\ D_e\ D_p \\ & \Big[-(n_p+1)\left(\frac{1}{2}+s\right) n_E\left(1-n_{E-E_p-E_m}\right) - n_p\left(\frac{1}{2}+s\right) n_E\left(1-n_{E+E_p-E_m}\right) \\ & -(n_p+1)\left(\frac{1}{2}-s\right) n_E\left(1-n_{E-E_p+E_m}\right) - n_p\left(\frac{1}{2}-s\right) n_E\left(1-n_{E+E_p+E_m}\right) \\ & +(n_p+1)\left(\frac{1}{2}-s\right) n_{E+E_p+E_m}\left(1-n_E\right) + n_p\left(\frac{1}{2}-s\right) n_{E-E_p+E_m}\left(1-n_E\right) \\ & +(n_p+1)\left(\frac{1}{2}+s\right) n_{E+E_p-E_m}\left(1-n_E\right) + n_p\left(\frac{1}{2}+s\right) n_{E-E_p-E_m}\left(1-n_E\right)\Big]. \end{aligned} \tag{4.33}$$

The $\left(\frac{1}{2}+s\right)$ terms are the probability of a transition from the $S_z = +\frac{1}{2}$ level to the $S_z = -\frac{1}{2}$ level, decreasing the energy of the electron, increasing the energy of the spin-system and reducing the average spin per atom s. The probability of the transition increases with the occupation of the lower level. Equation 4.33 can also be rewritten to give the rate of change of the average spin

$$\begin{aligned}\frac{\mathrm{d}s}{\mathrm{d}t} = {} & \frac{\alpha_{sf}\ K_{ep}\ D_e^2\ D_p}{D_m} \\ & \int \Big[-(n_p+1)\left(\frac{1}{2}-s\right) n_E\left(1-n_{E-E_p+E_m}\right) - n_p\left(\frac{1}{2}-s\right) n_E\left(1-n_{E+E_p+E_m}\right) \\ & +(n_p+1)\left(\frac{1}{2}+s\right) n_E\left(1-n_{E-E_p-E_m}\right) + n_p\left(\frac{1}{2}+s\right) n_E\left(1-n_{E+E_p-E_m}\right)\Big]\ \mathrm{d}E. \end{aligned} \tag{4.34}$$

Furthermore, the rate of change of the phonons is also influenced by the addition of this channel. Equation 4.32 is now added to an equation very similar to equation 4.34

$$\begin{aligned}\frac{\mathrm{d}n_p}{\mathrm{d}t} = {} & (1-\alpha_{sf})\ K_{ep}\ D_e^2 \int \left[(n_p+1)\, n_E\left(1-n_{E-E_p}\right) - n_p\, n_E\left(1-n_{E+E_p}\right)\right] \mathrm{d}E \\ & +\alpha_{sf}\ K_{ep}\ D_e^2 \\ & \int \Big[(n_p+1)\left(\frac{1}{2}-s\right) n_E\left(1-n_{E-E_p+E_m}\right) - n_p\left(\frac{1}{2}-s\right) n_E\left(1-n_{E+E_p+E_m}\right) \\ & +(n_p+1)\left(\frac{1}{2}-s\right) n_E\left(1-n_{E-E_p-E_m}\right) - n_p\left(\frac{1}{2}-s\right) n_E\left(1-n_{E+E_p-E_m}\right)\Big]\ \mathrm{d}E. \end{aligned} \tag{4.35}$$

4.4.3 Background on α_{sf}

If one considers the spin-flip scattering rate equation (4.33) carefully, the dissymmetry of the factors D_m and D_p could be a concern for the validity of this equation. However, the factor D_m missing from this equation, is absorbed into α_{sf} in order to keep the definition of α_{sf} intact. By absorbing D_m, the spin-flip parameter reflects the ratio of spin-flip and non spin-flip processes.

The spin-flip parameter α_{sf} can also be related to the Elliot-Yafet spin-flip probability α_{sf}. Consider a process in which N e-p events occur per unit of time. Of these N e-p events there

will be $\alpha_{sf}N$ spin-flip processes by way of definition of α_{sf}. The momentum scatter time τ is equal to $1/N$, and the spin-flip time T_1 is equal to $\frac{1}{\alpha_{sf}N}$. α_{EY} is defined as

$$\alpha_{EY} = \frac{\tau}{T_1} = \frac{\alpha_{sf}N}{N} = \alpha_{sf} \tag{4.36}$$

This result means that the microscopic model can directly be compared to the estimate of section 4.3, i.e. the upper boundary for α_{sf} is approximately 0.1.

4.5 Analytical solution

In order to develop physical understanding, we first discuss an analytical solution of the model. This can be achieved if we assume the electron system to be in constant internal equilibrium, i.e. we assume infinitely fast equilibration of the electron system, $\tau_{th} = 0$. Then the electron system is always a Fermi-Dirac distribution, described by a single parameter, the electron temperature T_e.

Also, the analytical model cannot be expanded to consider a changing exchange splitting, because the exchange energy is then dependent on the average spin. Taking this dependence into account in a self-consistent way no longer allows for a simple analytical solution.

In this section we will calculate analytically the most important parameters (τ_E, τ_M) of the simple model, and compare these to the parameters as fitted from the transients produced with the numerical simple model. Because of the fact that the Boltzmann differential equations, used in the dynamics, are not analytically solvable with respect to time, no transients of the electron, lattice, and spin temperature can be calculated. However, at $t = 0$, the moment the electron temperature is instantly increased (simulating the laser pulse), the values can be computed. For a purely exponential process the values calculated using the derivative at $t = 0$ will exactly correspond to the decay constant. The e-p equilibration is expected to be a (nearly) exponential decay, as predicted by the (S)3TM. For the demagnetization time, τ_M, this will in general not be the case, and several methods of calculation will be explored.

4.5.1 Calculation of τ_E

τ_E can be calculated by estimating the number of phonons necessary to equilibrate the electrons and the lattice and divide this number by the phonon creation rate at the moment of the laser excitation.

First consider the case of pure e-p relaxation ($\alpha_{sf} = 0$). Combining the phonon creation rate equation (4.32) with the equations for the Fermi-Dirac and Bose-Einstein distributions (4.20, 4.22) we find up to second order in the phonon energy E_p

$$\frac{\mathrm{d}n_p}{\mathrm{d}t} = K_{ep}D_e\left(T_e - T_l\right)\left[k_B - \frac{E_p^2}{12k_BT_eT_p}\right], \tag{4.37}$$

Before laser excitation ($t < 0$), the electron- and lattice-temperatures will be equal ($T_e = T_p = T_0$). At the moment the laser pulse strikes the sample ($t = 0$), the electron temperature is instantly increased from T_0 to $T_0 + \Delta T$, at this moment the lattice is still "cold", i.e. $T_l = T_0$. The total number of phonons per atom necessary to equilibrate the two systems to the final situation ($T_e = T_l = T_\infty = T_0 + \frac{c_l}{c_e+c_l}\Delta T$) is

$$\Delta n_p = \frac{c_l}{c_e + c_l}\Delta T\frac{\mathrm{d}n_p}{\mathrm{d}T_p}, \tag{4.38}$$

with

$$\Delta T = \left(T_e - T_p\right)|_{t\leq 0}. \tag{4.39}$$

From equation 4.38 and the phonon emission rate 4.37 the e-p equilibration time can be calculated, by taking the phonon emission rate constant at $t = 0$, i.e. $\dot{n}_p(t) = \dot{n}_p(t = 0)$.

$$\tau_E = \frac{\Delta n_p}{\dot{n}_p|_{t=0}} \tag{4.40}$$

Up to second order in the phonon energy E_p we find

$$\tau_E = \frac{c_l}{c_e + c_l} \frac{1}{D_e^2 K_{ep}} \left[\frac{1}{E_p} - \frac{\Delta T E_p}{12 k_B^2 T_0^2 (\Delta T + T_0)} \right], \tag{4.41}$$

The e-p equilibration time (τ_E) decreases with increasing phonon energy because of increasing efficiency in transferring energy from electrons to the lattice. However, with increasing phonon energy there are fewer available modes (Bose-Einstein) and the the efficiency will stagnate giving rise to the asymptotic behavior.

Actually, this curve would be a little more exaggerated if the e-p scattering cross section had also been included in the calculation, because of the higher scattering rate at higher phonon energies due to the dependence of K_{ep} on the phonon energy.

A similar result can be obtained if the spin-system is added to this calculation. The phonon excitation rate equation is the only change compared to the above calculation. Using equation 4.35 we can calculate $\dot{n}_p$ analogous to equation 4.37. Up to second order in both phonon energy and magnon energy we find

$$\frac{\mathrm{d}n_p}{\mathrm{d}t} = D_e^2 k_B K_{ep} \Delta T \left[1 - \frac{\alpha_{sf}}{4 k_B^2 T_0 (\Delta T + T_0)} E_m^2 - \frac{1}{12 k_B^2 T_0 (\Delta T + T_0)} E_p^2 \right]. \tag{4.42}$$

This leads to a τ_E of

$$\tau_E = \frac{c_l}{c_e + c_l} \frac{1}{D_e^2 K_{ep}} \left(\left[1 + \frac{\alpha_{sf} E_m^2}{4 k_B^2 T_0 (\Delta T + T_0)} \right] E_p^{-1} - \frac{\Delta T}{12 k_B^2 T_0^2 (\Delta T + T_0)} E_p \right). \tag{4.43}$$

This equation simplifies to equation 4.41 for $\alpha_{sf} \to 0$. The dependence on the phonon energy has not changed with respect to equation 4.41, only a term quadratic in the magnon energy has appeared. This is because not only the probability of magnon excitation increases, but also the heat capacity of the magnon system is increased, so more energy is required to equilibrate the magnon system to the other systems.

4.5.2 Calculation of τ_M

With equation 4.34 the equilibrium magnetization (average spin per atom) can be calculated by setting $\dot{s} = 0$, and setting $T_p = T_e = T_0$

$$s_{eq.} = -\frac{1}{2} \tanh \frac{E_m}{2 k_B T_0}. \tag{4.44}$$

This is the well known paramagnetic limit, known to describe a ferromagnetic system only at very low temperatures (see figure 4.11). This model ceases to be valid at the sharp bend (at approximately 50 K, for $E_m = 50$ meV). Also clearly visible for high temperatures is the lack of a critical point.

The demagnetization time τ_M can, analogously to equation 4.40, be calculated by dividing the number of needed magnon excitations to reach equilibrium by the magnon excitation rate at $t = 0$

$$\tau_M = \frac{\Delta s}{\dot{s}|_{t=0}}, \tag{4.45}$$

with

$$\Delta s = \frac{\mathrm{d}s(T)}{\mathrm{d}T} \Delta T, \tag{4.46}$$

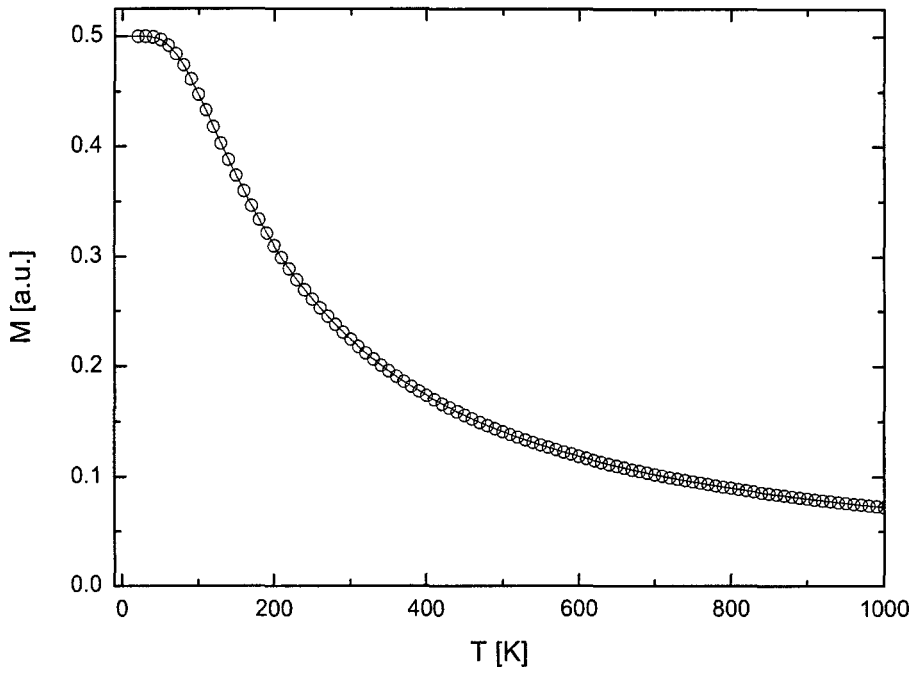

Figure 4.11: Equilibrium magnetization versus temperature of a two level magnetic system with a constant splitting of the energy levels. The solid curve is the analytical solution (eq. 4.44), the circles are points obtained by simulation with the simple model. This solution is only valid at very low temperatures.

where $s\,(T)$ is the equilibrium magnetization versus temperature curve.

Under the condition $s = s_{eq.}$, an analytical estimate can be made for the magnon emission rate at variable electron and lattice temperature. By substitution of the Fermi-Dirac (equation 4.20) and Bose-Einstein (equation 4.22) distributions into equation 4.34 we find up to second order in both phonon and magnon energies

$$\dot{s} = \frac{D_e^2\, K_{ep}\, D_p\, \alpha_{sf}\, k_B\, \Delta T}{D_m} \left[\frac{1}{E_p} + \frac{\Delta T - 2T_0}{12 k_B^2 T_0^2\, (\Delta T + T_0)} E_p \right] E_m, \tag{4.47}$$

with $T_p = T_0$ and $T_e = T_0 + \Delta T$.

This equation displays a few important trends. Firstly, in the case of thermal equilibrium ($\Delta T = 0$), it reduces to zero. Secondly, the magnon emission rate is inversely proportional to the phonon energy for small phonon energies. This means that even though low energy phonon modes have less chance to interact with an electron (see equation 4.30), these low energy modes are still very important for demagnetization. The reason for this behavior is the fact that when only low energy modes are available, the energy transfer from electron system to lattice system stagnates. Therefore, the energy transfer has to take place via the spin system, giving rise to a higher magnon emission rate. Thirdly the magnon emission rate increases if a higher energy magnon mode is used for scattering. This is to be expected because of the increase in efficiency in transferring energy from the electron system.

In the calculation of τ_M two cases can be distinguished.

a. Spin-relaxation is much slower than e-p equilibration. In this case the electron and phonon system are already in equilibrium before the spin system is changed appreciably. The number of required magnons to equilibrate the spin system with both the electron and

lattice systems can be calculated by

$$\Delta s = \frac{\mathrm{d}s_{eq.}}{\mathrm{d}T}\frac{c_l}{c_e + c_l}\Delta T, \tag{4.48}$$

with ΔT the initial temperature rise of the electron system. In this approach the influence of the spin heat capacity, c_s on the final temperature, is neglected, because at ambient temperatures the spin heat capacity is only approximately 10% of the total heat capacity. Furthermore, at higher temperatures c_s displays a $1/T$ dependence, diminishing its role even further.

The magnon excitation rate, $\dot{s}$, can be found by substituting $s = s_{eq.}$ and $T_e = T_p = T_0 + \frac{c_l}{c_e+c_l}\Delta T$, the final temperature of the electron and lattice systems, into equation 4.34. The demagnetization time τ_M can then be found by $\tau_M = \Delta s/\dot{s}$

$$\tau_{M,slow} = \frac{(c_e + c_p)\, D_m}{4D_e^2 D_p K_{ep} k_B^2 T_0 \left(c_l \Delta T + (c_e + c_p)\, T_0\right) \alpha_{sf}} \left[1 - \frac{2c_l \Delta T + (c_e + c_p)\, T_0}{12 k_B^2 T_0^2 \left(c_l \Delta T + (c_e + c_p)\, T_0\right)} E_m^2\right] E_p. \tag{4.49}$$

τ_M shows (inversely) the same trends as equation 4.47. The demagnetization time decreases with decreasing phonon energy, and decreases with increasing magnon energy (minus sign).

This equation is valid for spin-relaxation much slower than e-p equilibration, so for low values of α_{sf}, E_m, and high values for E_p. In this case the spin temperature displays simple exponential behavior, and the decay constant found with the analytical estimate is exact.

b. Spin-relaxation is much faster than e-p equilibration. The spin system will equilibrate with the electron system and then both systems will equilibrate with the lattice system.

The number of magnons necessary for equilibration can be calculated by

$$\Delta s = \frac{\mathrm{d}s_{eq.}}{\mathrm{d}T}\Delta T \tag{4.50}$$

and the magnon excitation rate by substituting $s = s_{eq.}$, $T_p = T_0$ and $T_e = T_0 + \Delta T$ into equation 4.34. The demagnetization time is this case is

$$\tau_{M,fast} = \frac{D_m}{4D_e^2 D_p k_B^2 K_{ep} T_0^2 \alpha_{sf}} \left[1 - \frac{2\Delta T + T_0}{12 k_B^2 T_0^2 \left(\Delta T + T_0\right)} E_m^2\right] E_p. \tag{4.51}$$

Equation 4.51 is only valid for high values of α_{sf}, E_m and low values for E_p. Because of this fast equilibration with the electron system, the spin temperature will follow the electron temperature, and will therefore display double exponential behavior (exponential relaxation towards a higher temperature followed by exponential relaxation to the equilibrium temperature). This means that the analytically calculated demagnetization time will not be exact.

Comparing both cases reveals an unexpected result;

$$\frac{\tau_{M,slow}}{\tau_{M,fast}} = \frac{(c_e + c_l)\, T_0}{c_l \Delta T + (c_e + c_l)\, T_0}. \tag{4.52}$$

Thus, if the spin-relaxation proceeds faster than e-p equilibration the demagnetization is actually **slower** than vice versa! This strange behavior, which is not physics, but just the failure of the simple analytical estimate, is caused by the much larger number of spins which will have to be flipped when equilibrating with the "hot" electron system, which will obviously increase with higher pump-induced temperature differences (ΔT). Hence the factor $c_l \Delta T$ making the difference in equation 4.52.

4.6 Weiss model

Looking at the magnetization versus temperature behavior of the simple model, it is clear that this model cannot be used to fit the measurements of van Kampen or Hohlfeld. The measurements of van Kampen take place at a temperature range of 300 K - 400 K, where the simple model equilibrium magnetization has a different behavior than the experimentally found behavior. For the measurements of Hohlfeld (heating above T_C) this model is not applicable at all, because there is no critical point. Hence, the next steps in modelling the demagnetization process should be to introduce a more realistic equilibrium magnetization, including a critical temperature.

In order to introduce the correct equilibrium magnetization behavior, the most simple model containing a critical point is incorporated, namely the Weiss model for magnetism. This model is a mean field model, i.e. one specific or tagged spin is considered in the field of all other spins. The field a specific spin feels as a result of all other spins is

$$H_{ex} = \lambda \left(n_{\sigma,\uparrow} - n_{\sigma,\downarrow} \right) = 2\lambda D_m s, \tag{4.53}$$

with H_{ex} the exchange field, and λ a constant, independent of temperature. The energy difference of the spin-up and spin-down state is

$$E_m = g\mu_B H_{ex} = 2g\mu_B \lambda D_m s. \tag{4.54}$$

This equation is very important; it links the magnon energy to the average spin, while the magnon excitation rate equation (4.34) relates the change of the average spin to the magnon energy. This means the exchange splitting between the spin-up and spin-down state will decrease with the decrease of the average spin (see figure 4.12). Also, because the average spin is linked to the exchange splitting, the energy of all other spins is changed whenever one spin is flipped. This is important because, if not properly taken into account, it introduces a violation of conservation of energy.

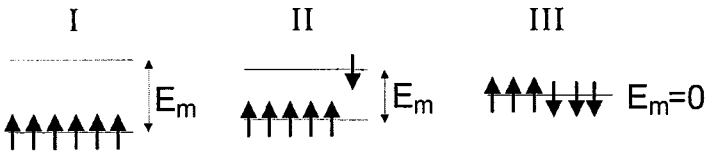

Figure 4.12: Average spin dependence of the exchange splitting of a magnetic two-level system. I. All spins are in the spin-up state, E_m is maximal. II. One spin is flipped reducing the exchange splitting E_m, but also the energy of both levels. III. Half the spins have been flipped, reducing E_m to zero.

To keep the energy-balance, the change in the total energy of all the spins has to be considered. Actually, this change in energy is caused by the shift of the electronic levels. Hence it makes sense to require the scattering electron to transfer this extra energy from or to the electron-system. This extra energy can be calculated by taking the zero point of the energy exactly in the middle of the two spin-levels (see figure 4.13). The energy of the spin-up and spin-down levels are half the spin-flip energy

$$E_\uparrow = -g\mu_B \lambda D_m s, \tag{4.55}$$
$$E_\downarrow = g\mu_B \lambda D_m s. \tag{4.56}$$

The total energy of the spin-system is given by

$$\begin{aligned} U_m &= \left(E_\uparrow n_{\sigma,\uparrow} + E_\downarrow n_{\sigma,\downarrow} \right) \\ &= \left[-g\mu_B \lambda D_m s \left(D_m \left(\frac{1}{2} + s \right) \right) + g\mu_B \lambda D_m s \left(D_m \left(\frac{1}{2} - s \right) \right) \right] \\ &= -2g\mu_B \lambda D_m^2 s^2. \end{aligned} \tag{4.57}$$

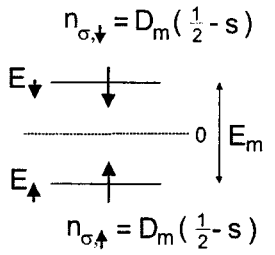

Figure 4.13: Two level spin system in the Weiss model; The energy levels $E_\uparrow$ and $E_\downarrow$ are dependent on the average spin.

The change of the total energy in the spin system as a result of a small change in average spin is

$$\frac{\mathrm{d}U_m}{\mathrm{d}s} = -4g\mu_B\lambda D_m^2 s. \tag{4.58}$$

Equation 4.54 gives the energy needed to flip one spin, but in equation 4.58 we calculate the flip of D_m spins. Multiplying equation 4.54 with D_m we see that this gives exactly half the total energy change of the spin system. Thus in the Boltzmann equations in the Weiss-model every instance of E_m has to be changed to $2E_m$.

Also, in equation 4.54 the physical meaning of the λ parameter becomes clear. With decreasing average spin, it becomes energetically increasingly easier to flip spins, and when the average spin is equal to zero we have arrived at a critical point, the Curie temperature. This means λ is a measure of the Curie temperature. From mean field theory [3] it is found that

$$\lambda = \frac{T_C}{C}, \tag{4.59}$$

with C the Curie constant, which can be determined by quantum theory for paramagnetism (high temperature boundary condition for the ferromagnetic/ paramagnetic transition), and is given by [3]

$$C = \frac{Ng^2\mu_B^2}{4k_B} \tag{4.60}$$

With these changes the equilibrium magnetization versus temperature behavior can again be investigated, the results are shown in figure 4.14.

By introducing the Weiss model for magnetism into the simple model investigated in the previous sections, it becomes necessary to develop numerical models, to be able to solve the Boltzmann equations.

4.7 Discretization Issues

In the implementation of the numerical models a number of discretizations are needed. For the implementation of the electron-electron (e-e) scattering the electron system is discretized with a mesh size ΔE (see figure 4.15(a)). The model considers an energy window of 2.5 eV around the Fermi-level. However, due to the nature of this scattering process it is numerically very expensive to take small mesh sizes (compare example 3). The mesh size used for e-e scattering is not that crucial, although precision increases with decreasing mesh size, it has been found that a mesh size of 50 meV is sufficient.

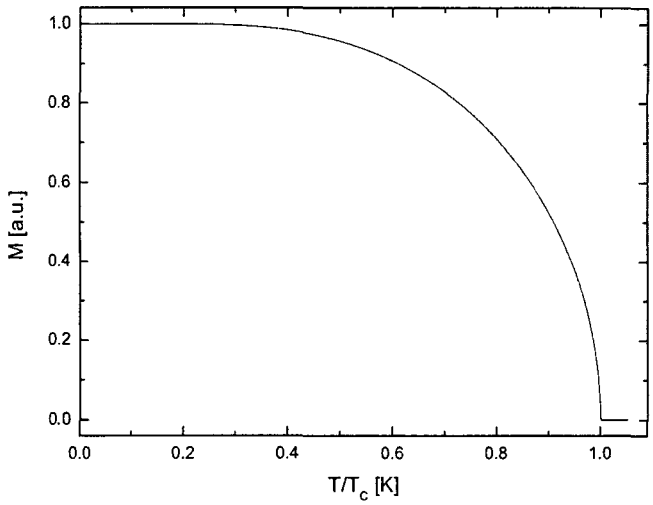

Figure 4.14: Equilibrium magnetization versus temperature in the Weiss. At approximately 575 K, for this case, a critical point (Curie temperature) is encountered. Above this temperature no more ferromagnetic behavior is encountered.

Example 3
Consider the Boltzmann equation for the electron-electron scattering process 4.28. For every energy band in the electron system a probability exist of scattering to every other level, provided there is enough energy available between the two scattering electrons to access unoccupied states. This means the calculation is roughly proportional to N^3, with N the number of subdivisions in the electron system, inversely proportional to the mesh size. Although some symmetries can be exploited to diminish the number of calculations, this is numerically a very expensive process, increasing very rapidly with decreasing mesh size.

The electron-phonon processes are more critical with respect to mesh sizes. When the model is limited to phonon and magnon energies of exactly the mesh size no discretization problems occur. However, due to the average field dependence of the magnon energy in the Weiss model, this condition cannot hold. Furthermore, the mesh size cannot be adapted to equal the magnon energy because this is a continuous variable, and problems with respect to energy conservation are to be expected.

To circumvent this problem the mode with an energy which is a non-integer multiple of the mesh size, is constructed by an interpolation scheme (see figure 4.15(b)). In this interpolation scheme the magnon mode of the right energy is composed by a linear combination of two magnon modes with energies which are integer multiples of the mesh size. However, in this case the mesh size has to be decreased in order for the interpolation to be precise enough. It was found that a mesh size of 5 meV was sufficient to achieve convergence of the interpolation scheme.

4.8 Numerical models

The model sub-systems and dynamics from the previous sections have also been implemented numerically. This numerical approach was necessary for two reasons; first, to produce transients (electron-, lattice-temperature, average spin); the simple paramagnetic model of section 4.4 requires far less computational effort when solved numerically. Second, the Weiss model for

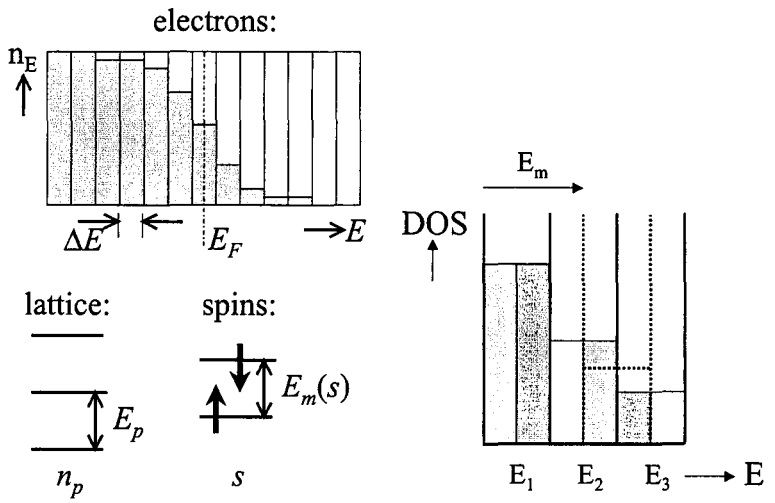

(a) Schematic depiction of the discretized system

(b) Interpolation scheme

Figure 4.15: Schematic depiction of the discretized system (a) and the interpolation scheme (b). The discretized system consists of the discretized electron system, with mesh size ΔE, the phonon system with constant energy E_p and the magnon system with average spin dependent magnon energy E_m. If the phonon or magnon energies are not integer multiples of the mesh size an interpolation scheme is necessary to calculate the transition rates. Consider a magnon energy of 1.5 times the mesh size; then the light grey part of the electrons at energy E_1 will scatter to E_2, while the dark grey part scatters to E_3. Thus, this magnon energy consists of a mode with energy ΔE and a mode with $2\Delta E$, while the occupation of the state the electrons scatter into is calculated by averaging (dotted lines). This method converges for small mesh size.

ferromagnetism is a self-consistent model, that cannot be solved analytically.

In total, four models were developed, namely

a. model I "Analytical"; a numerical implementation of the actual analytical model, i.e. with the same approximations. In this model the laser excitation, and subsequent e-e scattering were neglected (i.e. $\tau_{th} = 0$) in favor of an instant increase of the electron temperature, i.e. the electron system remains in equilibrium at all times. The main reason for the development of this model was the need for validation and comparison with actual analytical calculations.

b. model II "Simple"; the numerical implementation of the microscopic model described in section 4.4.

c. model III "Weiss"; the numerical implementation of the simple model, with the addition of the average spin dependent magnon energy, as described in section 4.6.

d. model IV "Loss"; the addition of heat conduction channels to the Weiss model implementation. This implementation was developed in order to increase the applicability of the microscopic model to different materials. Although this model was completed, no further tests were made.

The output of the numerical models are the macroscopic system parameters (electron temperature, lattice temperature, and average spin as a function of delay time). The electron temperature is determined by the derivative of the electron distribution at the Fermi-level

$$\left.\frac{\mathrm{d}n(E)}{\mathrm{d}E}\right|_{E_F} = \frac{1}{4k_B T_e} \tag{4.61}$$

The lattice temperature is calculated by adding the total energy of the excited phonons to the lattice total energy, and then converting back to temperature using the lattice heat capacity. The average spin is calculated by dividing the number of excited magnons per atom by the available number of magnons per atom (D_m).

To illustrate the dynamics of the numerical model, consider figure 4.16. The dynamics of the electron system are can be seen by the evolution of the electron distribution in figure 4.16(a), and the corresponding changes of the distribution in figure 4.16(b). At $t = 0$ the electron system is unperturbed, i.e. in a Fermi-Dirac distribution. As the laser pulse strikes the sample, an amount of electrons is excited to states above the Fermi level. Electron-electron scattering then rapidly restores a new Fermi-Dirac distribution at a higher temperature. When electron thermalization is completed, as a result of e-p and e-m scattering, the changes in the electron system will reverse direction at the Fermi-level.

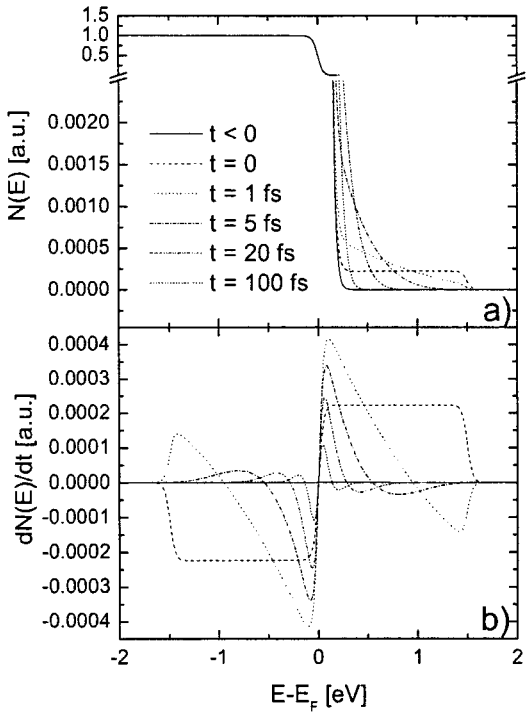

Figure 4.16: Electron densities (a) and changes in the electron densities (b) in the numerical model at various times. At $t < 0$ the system is unperturbed, the electrons are in a Fermi-Dirac distribution in equilibrium with both the lattice and spin system. At $t = 0$ the laser pulse ("smear"-excitation is used) excites a certain quantity of electrons (only the filling of the states is shown here). Then at different intervals the evolution towards a new Fermi-Dirac distribution at an elevated temperature can be observed. The changes in the electron system will diminish rapidly. Only when the thermalization process is completed, the changes in the electron system will reverse direction at the Fermi-level due to e-p and e-m scattering. For this simulation at an ambient temperature of 300 K, K_{ee} was chosen 1/3 fs^{-1}, a photon energy of 1.5 eV and $D_e = 2$ eV^{-1} was used.

Figures 4.17(a) and 4.17(b) display the typical curves produced by the numerical microscopic models. The difference between the magnetization behavior in figures 4.17(a) and 4.17(b) is caused by the choice of the spin-flip parameter α_{sf}. Figure 4.17(a) shows dynamics for a low value of the spin-flip probability α_{sf} (limit case of equation 4.49), and figure 4.17(b) shows transients for high values of α_{sf}.

In general, the transients look very similar to the dynamics of the three temperature model of section 2.3. Because of this similarity the same equations (2.15, 2.16 and 2.17) can be used to fit these curves and thereby extract the relevant timescales (also indicated in both figures).

However, due to the different behavior of the magnetization transient in figure 4.17(a) with

respect to the three temperature model, the spin-temperature equation (2.17) will not be able to fit this magnetization curve. For this case an equation of the form of the lattice temperature equation (2.16) must be chosen:

$$s(t) = s_0 + \Delta s \left[1 - e^{\left(-\frac{t}{\tau_M}\right)}\right], \tag{4.62}$$

with s_0 the equilibrium magnetization at $t = 0$ and Δs the resulting change in the magnetization in the final equilibrium situation.

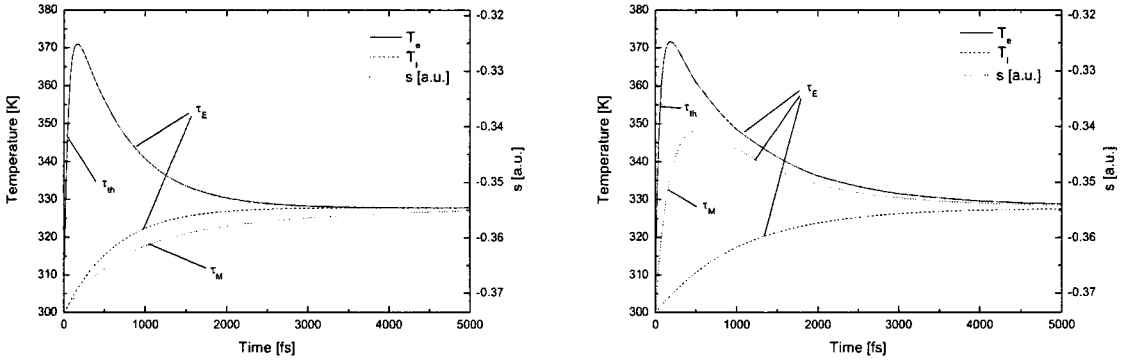

Figure 4.17: Transients of the simple microscopic model. The electron temperature is indicated by the solid line, the lattice temperature is the dashed line, and the average spin (right scale) is the dotted line. Subfigure (a) displays the average spin in the limit of equation 4.49, i.e. $\tau_M > \tau_E$ and subfigure (b) displays the limit of equation 4.51, i.e. $\tau_M < \tau_E$ (b).

4.8.1 Model parameters

In order to model ferromagnetic nickel thin layers (experimented on by van Kampen *et al.* and Hohlfeld *et al.*), the parameters of the models have to be chosen in accordance. For most parameters experimental or literature values are known. In this section the used parameters will be presented, and in further sections, only deviations from this parameter set will be mentioned.

Electron system and electron-electron scattering

For the electron system only two parameters are used; the density of states, and K_{ee}, the e-e scattering probability. As previously mentioned in section 4.4.2, E_F^2/K_{ee} was determined from experiment, and with $E_F \approx 9$ eV for nickel, K_{ee} is equal to 27 fs^{-1}. The density of states, D_e, was chosen constant and estimated from an average of the actual density of states, which is approximately 2 $\text{eV}^{-1}\text{at}^{-1}$.

Lattice system and electron-phonon scattering

The lattice system has slightly more parameters; The lattice heat capacity is chosen according to the ratio of electron- and lattice- heat capacities found in the experiments by van Kampen. Van Kampen *et al.* found a value of $c_l = 2.8 \cdot 10^6$ $\text{Jm}^{-3}\text{K}^{-1}$ for the lattice heat capacity and $c_e = \gamma T_e = 1.13 \cdot 10^6$ $\text{Jm}^{-3}\text{K}^{-1}$ electronic heat capacity, at room temperature, yielding a ratio of $c_l/c_e = 2.48$.

Because in the microscopic model the electronic heat capacity is fixed by the density of states, the lattice heat capacity was scaled in order to reproduce this experimental heat capacity ratio,

and thus the correct dynamics. By this procedure a heat capacity of $c_l = 3.51 \cdot 10^{-5}$ eVK^{-1}at^{-1} was found.

By transient reflection studies by van Kampen on nickel thin layers, the e-p equilibration time τ_E could be determined, and was found to be approximately 0.6 ps. The microscopic model should therefore reproduce this value. However, τ_E is determined by several parameters. Consider the phonon excitation rate equation (4.35), from this equation it is clear that τ_E will be dependent upon K_{ep}, α_{sf}, E_p and E_m. Therefore, it seems most prudent to scale K_{ep} to reproduce τ_E, when suitable values for the others parameters have been found.

The density of modes of the phonons is chosen to be $D_p = 1$, the electrons only scatter with longitudinal phonons. As mentioned in section 4.4.2, only one phonon mode is considered for scattering, and because the scattering cross-section depends linearly on the phonon energy, the phonon energy is chosen equal to $E_p = k_B\Theta_D$. For nickel the Debye temperature is reported to be around 450 K, so $E_p \approx 36$ meV. Then, for $\alpha_{sf} = 0$, K_{ep} must be chosen $1.64 \cdot 10^{-3}$ fs^{-1}eV^{-1} to reproduce $\tau_E = 0.6$ ps.

Spin system and electron-phonon scattering with spin-flip

For the spin-system two parameters are of importance; the magnon energy or exchange splitting E_m (which determines the critical temperature) and the number of available magnon modes per atom, D_m.

This last parameter influences the heat capacity of the spin system c_s, by

$$c_s = \frac{\mathrm{d}}{\mathrm{d}T} n_{\sigma\downarrow} E_m = g\mu_B \lambda D_m^2 (1 - 4s) \frac{\mathrm{d}s}{\mathrm{d}T} \tag{4.63}$$

The magnetic heat capacity of nickel has been experimentally determined to be about 10% of the total heat capacity [2], increasing with temperature until the Curie temperature, and then dropping steeply. In order to get a 10% heat capacity of the spin system, the number of available magnon modes per atom were determined to be $D_m \approx 0.08$ at^{-1}. This is a deviation from the literature value of 0.6 μ_B per atom [3].

The parameters in the electron-phonon with spin-flip process are the magnon energy, E_m and the spin-flip scattering probability, α_{sf}. The magnon energy can be determined by the exchange splitting of the d-band, which is responsible for nickel's ferromagnetic behavior. For calculated bandstructures (e.g. figure 4.7(c)) an exchange splitting is found in the region of $E_m \approx 750$meV. However, it is known from experimental studies that bandstructure calculations usually overestimate the exchange splitting. From the Weiss model for magnetism also an estimate can be made. The relation between the Curie temperature and the exchange splitting is given by

$$\Delta = 2k_B T_c. \tag{4.64}$$

Nickel has a Curie temperature of approximately 624 K, resulting in an exchange splitting in the order of 100 meV. In all calculations, $E_m = 100$ meV was used.

The spin-flip scattering parameter, α_{sf}, is the crucial parameter about which we hope to learn more by comparing simulation to experiment. Calculated values for nickel are not available in literature. By definition $0 \leq \alpha_{sf} \leq 1$, but values higher than 0.5 are considered highly unrealistic. In conjunction with K_{ep}, keeping τ_E constant, α_{sf} can be used to fit the magnetization dynamics as measured by van Kampen *et al.* or Hohlfeld *et al.*. Also, an estimate of α_{sf} can be made on the basis of section 4.3, and K_{ep} scaled accordingly.

4.8.2 Validation

In order to check the numerical models, a numerical model (model I) was developed using the same approximations as the analytical model (electron system remains in constant equilibrium). Due to the mismatch of heat capacities between the two models, the analytical calculations yield

structurally longer dynamics. In the analytical calculations the characteristic timescales (τ_E, τ_M) have been calculated using the derivative at $t = 0$ (e.g. $\frac{dT_e}{dt}$, see section 4.5), while in the numerical simulations these timescales were determined by fitting. It has been verified that in the numerical model the number of excited phonons and magnons were equal to the analytical model. Thus it is possible to scale the timescales.

Figure 4.18 shows τ_E and τ_M as a function of phonon energy and magnon energy for both analytical (solid line) and numerical model (open circles). The models show perfect agreement, validating the numerical model. This agreement was achieved after scaling, for τ_M a factor $5.73 \cdot 10^3$, and for τ_E a factor $6.56 \cdot 10^3$ was used.

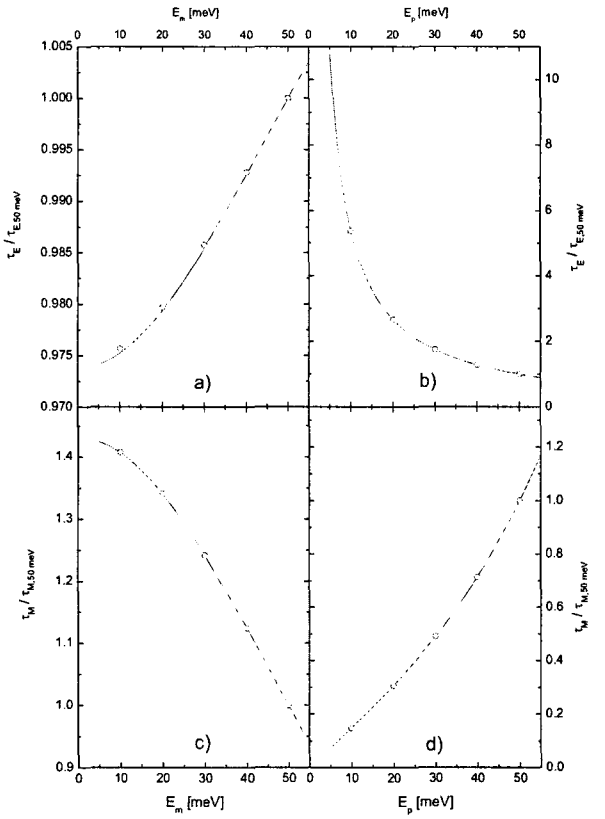

Figure 4.18: Comparison of the analytical model and the numerical model, with infinitely fast thermalization, i.e. laser excitation is implemented as a sudden increase of the electron temperature. The curves overlap perfectly after scaling, which was necessary because of heat capacity mismatch between the analytical and numerical models.

Furthermore, special care was taken to guard other models from accidental mistakes. The programming of the numerical models has been done in an object oriented fashion, thus assuring reuse of previously validated code.

4.9 Results & Discussion

In order to learn about the general behavior of the models, a number of parameters can be varied to simulate various experiments. Also, in this way some predictions can be made about experiments not yet carried out. Some of the trends predicted by the microscopic model are open to experimental verification. Of course, in experimental systems it will not be possible to vary most parameters independently.

4.9.1 α_{sf} dependence

In figure 4.19 the spin-flip probability α_{sf} is varied using model III (Weiss model). For sake of clarity the electron- and lattice-dynamics are displayed only for the case of $\alpha_{sf} = 0.1$. Clearly visible is the widely varying behavior of the magnetization transients. If α_{sf} is chosen below 0.1 the curves display a simple exponential decay, slower than the e-p equilibration process. If a value much higher than 0.1 is chosen for α_{sf} the magnetization dynamics present a double exponential behavior, yielding much lower demagnetization times. For this set of parameters ($E_p = E_m = 50$ meV and $D_m = 0.006$ at^{-1}), τ_M is not optimized for nickel. The actual values for nickel ($E_p \approx 36$ meV, $E_m \approx 100$ meV and $D_m = 0.08$ at^{-1}), yield demagnetization times which are slightly longer (not faster than the thermalization time, not even for $\alpha_{sf} = 1.0$).

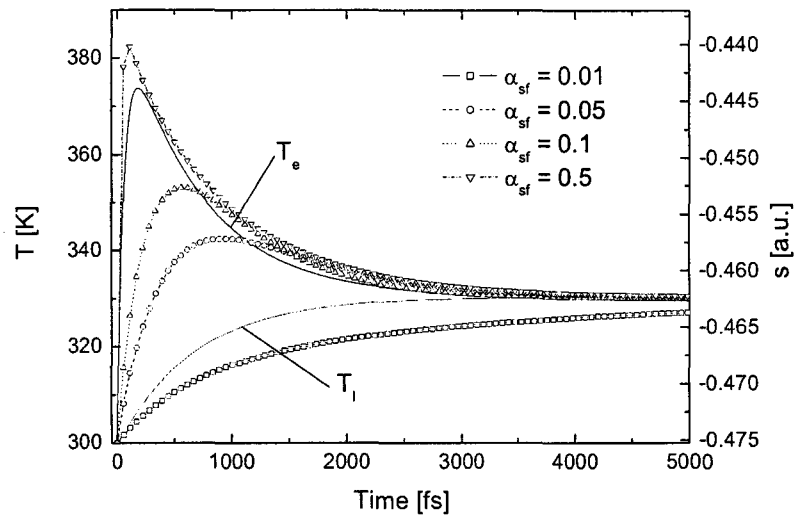

Figure 4.19: Magnetization as function of the spin-flip parameter α_{sf} in the simple model. The parameters ($E_p = E_m = 50$ meV and $D_m = 0.08$ at^{-1}) were chosen to achieve $\tau_M < \tau_{th}$.

The most impressive result of figure 4.19 is the fact that the demagnetization **can** be faster than e-p equilibration with a phonon mediated spin-flip mechanism. This disproves the claim often made in literature, that phonon based mechanisms are necessarily slower than e-p equilibration. Furthermore, it is shown that the demagnetization can even be faster than the thermalization time of the electron system, although this was achieved for unrealistic parameters.

4.9.2 Pump energy dependence

Another interesting feature of this model is the possibility to use high pump powers, that drive the temperature beyond the critical point. In figures 4.20 the results of such an experiment is shown. Especially the τ_M curve shows a spectacular variation with increasing pump power. The behavior of the τ_E curve is less pronounced, but the features of both curves suggest a connection with the critical point. After comparison with the equilibrium magnetization versus temperature (and thus needed pump power) curve, the Curie point for this experiment was found to be at a pump power of 7.7, i.e. a temperature of 580 K (dotted line in figure 4.20). In this simulation all parameters were chosen conform section 4.8.1, except for $E_p = 50$ meV. The explanation of the demagnetization time versus pump power curve is not that straightforward. The first part, the rise of the curve, can be explained by the fact that, more magnons have to be emitted, until the Curie temperature is reached. The decrease of the curve is caused by the increasing quantity of energy in the electron system, and thus leading to increasing probability of e-m scattering. This argument does not explain why the maximum of the τ_M curve does not coincide with the critical

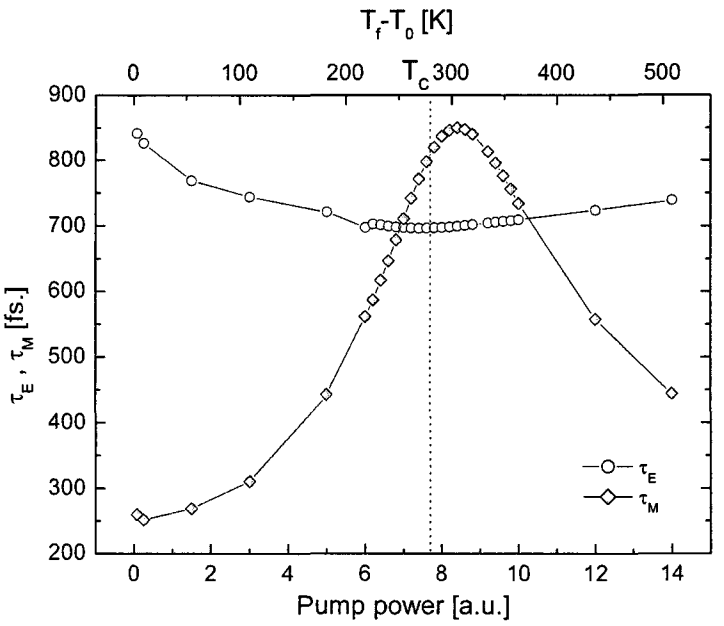

Figure 4.20: τ_E and τ_M as function of pump power at a starting temperature $T_0 = 300$ K, the dotted line indicates the critical temperature. The peak is caused by the increase of the number of magnons excitations needed as the temperature rises towards the critical point. Once the critical point is reached, the number of needed magnon excitations becomes constant. The decrease is caused by the large quantity of energy deposited in the electron system, giving rise to higher probability of e-m scattering.

temperature. However, it could be observed that the last part of the equilibration process in the vicinity of the critical temperature is very slow (no pure exponential behavior, see figure 4.21). Thus the fitted demagnetization time may be shorter than the actual τ_M.

These trends may be experimentally verified by pump energy dependent measurements of the reflectivity (yielding τ_E) and MOKE-experiments.

4.9.3 Phonon energy dependence

The primary phonon scattering energy can be varied by using materials with widely different Debye temperatures. Materials that obey the Debye model for phonons will be an even simpler verification, in this case only the lattice dimensions need to be varied. The behavior of the characteristic timescales (τ_M, τ_E) as function of phonon energy is displayed in figure 4.18(b) and (d).

4.9.4 Exchange energy dependence

The dependence of τ_M (and τ_E) on the exchange splitting, and thus scattering magnon energy, can be investigated by making a detailed study of different materials. Its origin lies in the balance of exchange energy and kinetic energy (Stoner criterion), and is therefore closely related to the density of states at the Fermi-level. The influence of the exchange splitting can be studied by varying a $Ni_{1-x}Cu_x$ alloy as a function of x. The behavior of the characteristic timescales (τ_M, τ_E) as function of phonon energy is displayed in figure 4.18(a) and (c).

Also, the spin scattering parameter α_{EY} is dependent on the density of states near the Fermi-level. The more electronic states are present near the Fermi-level, the greater the chance of close lying bands and accidental degeneracies, and hence more spin-flip scattering as argued

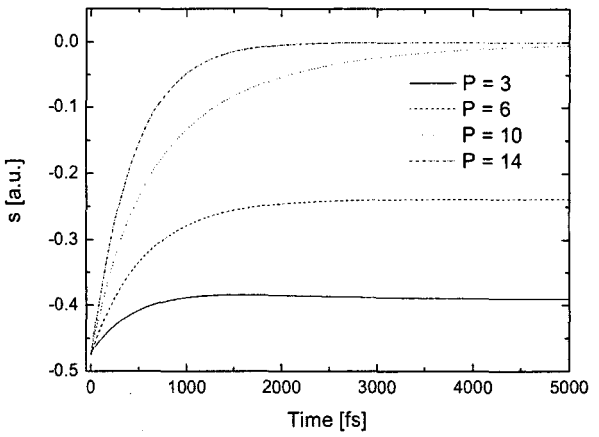

Figure 4.21: Average spin as function of pump power at a starting temperature $T_0 = 300$ K. Because of the differences in the shape of the curves, a simple exponential fit does not yield the correct demagnetization time in every case. Therefore, the peak in figure 4.20 may be shifted.

in section 4.3. It is also arguable that it is indeed the fact that nickel is ferromagnetic, is also the cause of its high spin-flip probability, which should also be verifiable with other ferromagnetic systems.

4.9.5 Ambient temperature dependence

Figure 4.22 shows the dependence of the demagnetization time on the ambient temperature. Since the demagnetization time is dependent on the slope of the equilibrium magnetization versus temperature curve (see equations 4.45 and 4.46), it is to be expected that the demagnetization time displays a similar behavior, i.e. asymptotic behavior towards the critical point.

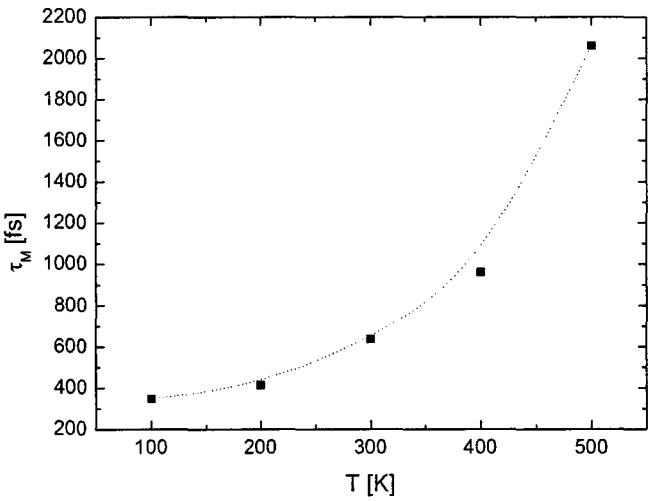

Figure 4.22: τ_M as function of ambient temperature, the dotted line is not a fit, it is intended as a guide to the eye. τ_M as function of temperature shows similar behavior as the equilibrium magnetization curve, i.e. asymptotic behavior towards the critical point.

However, due to fitting difficulties with the (double) exponential functions (see figure 4.23

the demagnetization time was calculated as in the analytical model:

$$\tau_M = \frac{\Delta s}{\dot{s}|_{t=0}} \tag{4.65}$$

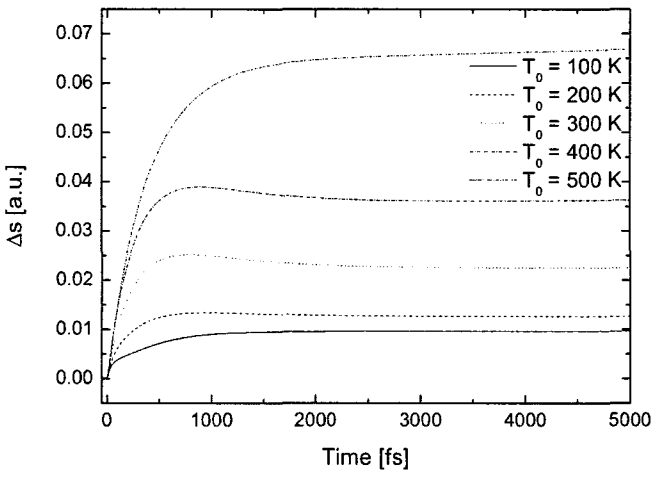

Figure 4.23: Average spin transients at different ambient temperatures, at constant pump powers. Due to the widely different shapes of the curves, it was not possible to obtain a consistent picture of the demagnetization time as function of ambient temperature.

For future studies the ambient temperature behavior of the model is of crucial importance. Such a study can be compared to the experimental data, and to the S3TM transients in order to check if the microscopic model is able to fit the measurements at three different temperatures simultaneously and if the fit is better than the three temperature model.

4.9.6 Fit to experimental data by van Kampen *et al.*

The Weiss model can be used to fit the measurements of van Kampen *et al.* after adaptation with the thermal difference methods, or iterative scheme. The measurements of van Kampen are particularly suited, since they also performed transient reflectivity measurements under equal conditions, yielding the electron temperature. Figure 4.24 shows the thermal difference solution ($T_s^{(1)}$, open squares), and the solution of the iterative scheme ($T_s^{(10)}$, open circles). Due to the calculation time involved in solving the numerical model, only an approximate fit has been made.

The values used in the fit are the parameters optimized for nickel as described in section 4.8.1, except for K_{ep}, which is approximately equal for both curves and has the value $K_{ep} = 1.78 \cdot 10^{-3}$. The most interesting parameter obtained from the fits is the spin-flip parameter α_{sf}. For the $T_s^{(1)}$ curve the spin-flip parameter was found to be $\alpha_{sf} = 0.06$ and for $T_s^{(10)}$ $\alpha_{sf} = 0.12$.

The values of α_{sf} found with this fit are in good agreement with the spin-flip probability as estimated from the hot-spot theory (see section 4.3). Also, although this is just an approximate fit, the numerical model fits the data at least as good as the three temperature model.

4.9.7 Energy diffusion

In view of future expansions to this model, energy diffusion is considered one of the more important additions. As discussed earlier (see section 4.8) a model (model IV) was developed to incorporate energy diffusion, however, no further work was done.

Energy diffusion from the studied magnetic layer to another layer can take place in two ways; via the lattice (isolator), and via the electrons (conductor). In the case of an isolating

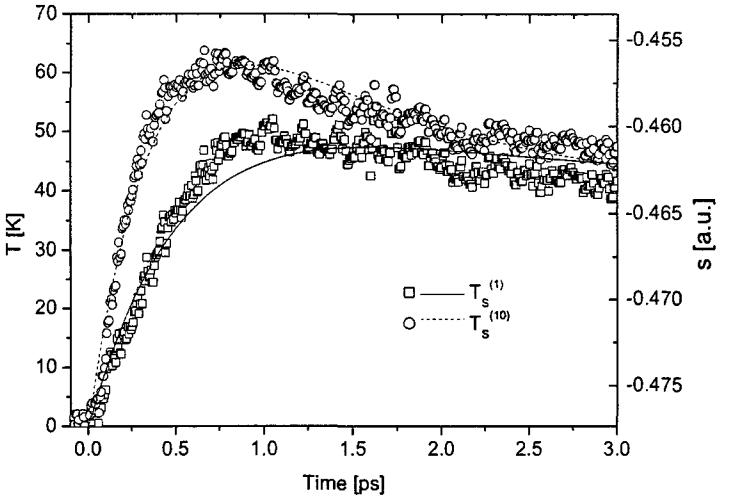

Figure 4.24: Microscopic model (model III) fit to the experimental data obtained with the macroscopic model of chapter 4. The open squares and circles indicate the results of the thermal difference scheme and iterative method respectively. The solid curves represent the (approximate) fits, made with the microscopic model. The fitted parameter α_{sf} was found to be 0.06 for the thermal difference data, and 0.12 for the iterative data, and in conformity with expectations obtained with the hot-spot model. The fits are at least as good as the S3TM-fits.

layer beneath the studied layer, there will only be very few available states for the hot electrons to diffuse to, so energy diffusion will happen through phonons. Because initially the lattice is "cold" it will take considerable time for energy diffusion to have a noticeable effect. This type of diffusion can be described by

$$\frac{\mathrm{d}T_l}{\mathrm{d}t} = \lambda_D \left(T_l - T_A\right), \tag{4.66}$$

with T_l the lattice temperature of the magnetic layer, λ_D the heat diffusion constant, and T_A the temperature of the second layer.

When the layer of interest is deposited on top of a conducting layer, energy diffusion will be much faster. Because of the high amount of available electronic states, a fast transport of hot electrons is expected, i.e. ballistic electron transport. The transport of the hot electrons is dependent on the electron distribution of the magnetic layer and the Fermi-Dirac function at the temperature of the conduction layer (assuming a continuous thermalized state). Because the layers do not get charged in the process, electrons of lower energy will make the reverse transition. This type of diffusion process can be described by an electron colliding with a diffusion quasi-particle

$$\frac{\mathrm{d}n_E}{\mathrm{d}t} = K_{ed} \int n_{E-E_d} n_{d,+} \left(1 - n_E\right) - n_E \, n_{d,-} \left(1 - n_{E-E_d}\right) \mathrm{d}E, \tag{4.67}$$

with K_{ed} the probability of diffusion, and

$$n_{d,-} = f\left(E - E_d\right)\left[1 - f\left(E\right)\right], \tag{4.68}$$

$$n_{d,+} = f\left(E\right)\left[1 - f\left(E - E_d\right)\right], \tag{4.69}$$

with $f\left(E\right)$ the Fermi-Dirac function. The temperature of the second electron system will have to be updated by calculating the temperature change of every event. When the temperature of both systems is equal, and the electron system of the magnetic layer is in equilibrium the diffusion will cease, because then all the terms in the integral cancel.

The addition of energy diffusion enables the model to be applicable to experimental systems in which cooling plays an important role. Furthermore, the paramagnetic-ferromagnetic transition can be investigated. Because with this model cooling can also be ultra-fast (depending on the choice of λ or K_{ed}), some predictions can be made concerning the recovery of the magnetization.

Moreover, with the addition of an external field, even ultra-fast switching can be investigated, due to the symmetry of the dynamic equations with respect to spin (see figure 4.25). An ultra-fast switching simulation works as follows: first a high power laser pulse heats the sample above the critical point, reducing the magnetization to zero. Then the sample is cooled while an external magnetic field is applied, switching and recovering the magnetization in the opposite direction.

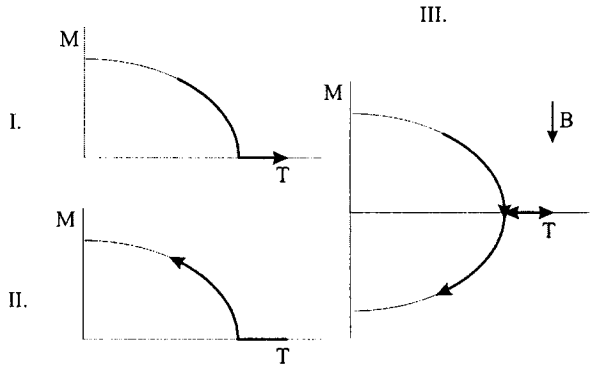

Figure 4.25: Schematic depiction of ultrafast switching. I. A high power laser pulse reduces the magnetization to zero. II. The sample is cools off recovering its magnetic moment. III. The switching experiment; step I. is followed by cooling in presence of a external magnetic field, recovering the magnetization in the opposite direction.

4.10 Conclusions

In this chapter a microscopic model was presented to account for ultra-fast demagnetization in ferromagnetic transition metals such as nickel. This model unlike others does not violate conservation of angular momentum.

Using the Elliot-Yafet and hot-spot theory for spin-orbit scattering, it was shown that nickel may have a substantially higher spin-flip scattering probability than is to be expected from a simple Z^4 estimate.

Because the dynamics of this model does not allow for a simple analytical solution, numerical models were developed. In the limit of infinitely fast electron thermalization these models were validated using analytical calculations.

The most important observation obtained from the model is that although the spin scattering is phonon mediated, it was shown that the demagnetization time can be shorter than e-p equilibration. The demagnetization could even be shorter than the thermalization time for optimized parameters. This disproves the claim often made in literature that the phonon based demagnetization is necessarily slower than e-p equilibration, and can therefore be disregarded in this process.

The demagnetization and e-p equilibration display a spectacular variation as a function of pump power. This variation occurs in the region of the critical point. Although the peak in the demagnetization time does not precisely coincide with the Curie point, the rise of the peak can be explained by the increasing number of magnons that have to be emitted to reach equilibrium. The decrease is then explained by the increasing energy in the electron system, giving rise to higher scattering probabilities.

The demagnetization and e-p equilibration are highly dependent on the energy of the primary scattering phonon mode. The higher the phonon energy, the faster e-p equilibration and the slower the demagnetization. Experimentally, this can be verified by investigating materials with a different Debye temperature in the low temperature regime.

Another material parameter that has large influence on the demagnetization is the exchange energy. Materials with a high exchange energy display a faster quenching of the magnetic moment. However, because the critical point of such a material is also higher, this will not mean a faster complete demagnetization.

The ambient temperature dependence of the demagnetization process was also investigated, yielding an asymptotic increasing demagnetization time with increasing ambient temperature. This behavior was expected because of the decreasing slope of the equilibrium magnetization versus temperature curve, yielding an increasing heat capacity. The ambient temperature behavior of the microscopic model is important for future research because the ambient temperature behavior of the model can be compared to the experimental data of van Kampen *et al.*

The TR-MOKE measurements of van Kampen *et al.*, after adaptation with the thermal difference and iterative schemes, were fitted with physically relevant parameters for nickel, yielding spin-flip probabilities, α_{sf}, of 0.06 and 0.12 respectively. This is in conformity with the expectations derived from the hot-spot theory.

An important extension of the model for further research is the possibility to include energy diffusion channels. Although these channels were implemented, no further simulations were done. This extension makes it possible to consider ultra-fast cooling, and if the model is also extended to include an external field, even ultra-fast switching can be considered.

Chapter 5

General conclusions

This thesis deals with two important issues in the field of magneto-optics. First, the microscopic explanation of the process responsible for ultra-fast (< 0.5 ps) demagnetization. Second, the interpretation of the Magneto Optical Kerr Effect (MOKE) with which this ultra-fast demagnetization is measured.

For the interpretation of the MOKE data a macroscopic model (iterative method) was developed to separate the magnetization dynamics from the optical contributions in the measured signal. Although the method failed due to extra non-linearities in the measured data, it is expected that the method may yield good results with data obtained with low pump-powers.

For the microscopic explanation a microscopic model was developed using phonon mediated spin-flip scattering, by assigning a spin-flip probability to every electron-phonon scattering event. In contradiction to claims in literature, it was proven that phonon mediated can be faster than electron-phonon equilibration (and for unrealistic parameters even faster than thermalization).

By fitting the microscopic model to data obtained with the macroscopic model, spin-flip probabilities were obtained that are in conformity with estimates made with the hot-spot theory.

Bibliography

[1] E. Beaurepaire, J.C. Merle, A. Daunois, and J.Y. Bigot. *Phys. Rev. Lett.*, 76:4250, 1996.

[2] M. van Kampen. *Ph.D. thesis, Eindhoven University of technology, The Netherlands; M. van Kampen et al., submitted to Phys. Rev. B.*, 2003.

[3] C. Kittel. *Introduction to solid state physics, 7th edition*, page 444, 1996.

[4] P.M. Oppeneer and A. Liebsch. *J. Phys.: Condens. Matter*, 16:5519–5530, 2003.

[5] G.P. Zhang and W. Hubner. *Phys. Rev. Lett.*, 85:3025, 1999.

[6] E. Beaurepaire, G.M. Turner, S.M. Harrel, M.C. Beard, J.-Y. Bigot, and C.A. Schmuttenmaer. *Appl. Phys. Lett.*, 84:3465–3467, 2004.

[7] J. Hohlfeld, E. Matthias, R. Knorren, and K.H. Bennemann. *Phys. Rev. Lett.*, 78:4861, 1997.

[8] R.J. Elliot. *Phys. Rev.*, 96:266–279, 1954.

[9] Y. Yafet. *Solid state physics*, 14:2–96, 1963.

[10] A. Einstein and W.J. de Haas. *Verhandl. Deuts. Phys. Ges.*, 17:152, 1915.

[11] J.Fabian and S. Das Sarma. *Phys. Rev. Lett.*, 81:5624–5627, 1998.

[12] P.Monod and F.Beuneu. *Phys. Rev. B*, 19:911–916, 1979.

[13] R.Coehoorn. *Novel Magneto-electronic Materials and Devices Lecture Notes TU/e 2001-2002*, page 44, 2002.

[14] M.Bauer and M.Aeschlimann. *Journal of Electron Spectroscopy and Related Phenomena*, 124:225, 2002.

[15] J.Hohlfeld. *Ph.D. thesis, Freien Universitaet Berlin, Germany, J.Hohlfeld*, 1998.